Environment, Stability and Acidity of External Surface Sites of Silicalite-1 and ZSM-5 Micro- and Nano-Slabs, -Sheets and -Crystals

Laureline Treps, Axel Gomez, Theodorus de Bruin, Céline Chizallet

Environment, Stability and Acidity of External Surface Sites of Silicalite-1 and ZSM-5 Micro- and Nano-Slabs, -Sheets and -Crystals

Laureline Treps,[†] Axel Gomez,[†,§] Theodorus de Bruin,[‡] Céline Chizallet[†,*]

[†] IFP Energies Nouvelles, Rond-point de l'échangeur, BP3, 69360 Solaize, France

[‡] IFP Energies Nouvelles, 1 et 4 avenue de Bois-Préau, BP3, 92852 Rueil-Malmaison, France

[§] Département de Chimie, École Normale Supérieure, PSL University, 75005 Paris, France

celine.chizallet@ifpen.fr

ABSTRACT: Zeolites are nanoporous aluminosilicate crystals of prominent fundamental and industrial importance. Among these, ZSM-5 is the most investigated solid that can be obtained in various forms, some of these (hierarchical forms, nanoslabs, nanosheets and nanocrystals) exhibiting a very high external surface over volume ratio. Whereas most knowledge obtained so far at the atomic level concerns the internal nanopores, we here propose a Density Functional Theory (DFT) study to establish the relative stability of relevant surface orientations for silicalite and ZSM-5 crystals ((100), (010) and (101)) at different hydration levels to identify the equilibrium morphology of the particles, and the major sites present on their surfaces. Several kinds of surface sites have been identified. Bridging Al-OH-Si groups are present at the pore mouth with similar or higher stability with respect to those in bulk sites. Yet, these groups are not stable at the outermost surface, where the following groups prevail: Si-OH, Al-OH groups, and most importantly water adsorbed on aluminum Al-$(H_2O)(OH)_n$. Water desorption reactions occur at temperatures that strongly depend on the local topology of the surface site and on the surface orientation: when a siloxane bridge is present below the surface Al atom, water desorption is promoted by the formation of an additional Al-O bond with the oxygen of the siloxane bridge. However, if such bridge is not present below the surface aluminum atom, desorption leads to a less stable surface Al_{III} atom. The desorption temperature is influenced by this feature, as well as by the stabilization of the water molecule by hydrogen bonds, depending on the silanol content of the surface. This has in turn direct consequences on the Brønsted and Lewis acid properties, as probed by pyridine. Strong Lewis acid sites can easily be formed on the (010) orientation (relevant for nanosheets), whereas they are unlikely to occur at the (101) surface (tips of coffin-shaped particles), which promotes mild Brønsted acid sites Al-(H_2O) instead.

KEYWORDS: zeolites, external surface, acid sites, pyridine, Density Functional Theory

1. INTRODUCTION

Zeolites are nanoporous (historically called "microporous") aluminosilicates with a well-defined crystalline structure. They can be described as a rigid three-dimensional network of TO_4 tetrahedra (where T is mostly Si). These tetrahedra are linked at their corner via a common oxygen atom to form a secondary building unit (SBU). The presence of Al^{3+} cations in crystallographic positions otherwise occupied by Si^{4+} is compensated in terms of charge by extra-framework cations, conferring a large array of properties such as ion exchange, gas separation and catalysis.[1-2] In particular, zeolites are widely employed in refining and petrochemical processes, resulting from their particular properties, such as high adsorption capacity, hydrothermal stability, shape selectivity and intrinsic (Brønsted and Lewis) acidity.[3-5] They are also used in pollution abatement,[6-8] and are promising candidates for biomass conversion.[9]

The well-defined crystalline structure of zeolites, together with the large diversity of pore architectures, at the origin of tunable confinement effect,[10] allow designing of catalysts and adsorbents from structural considerations.[8,11-12] Indeed, more than 230 zeolite structures (natural and synthetic) have been identified and are listed on the International Zeolite Association (IZA) website.[13] Moreover, in the case of proton as compensation cation that we will consider further, it is known for decades that bridging Si_{IV}-OH-Al_{IV} hydroxyls are the Brønsted acid sites in the microporosity.[14-16] Much less information is available on the nature of the sites accessible at the external surface of the crystallites. This is, however, a crucial information in several contexts. First, the "pore-mouth

catalysis" was invoked to take place – with a specific reactivity at the external surface – for zeolites which pores are smaller than the bulky molecules to be converted.[17-18] Secondly, some recent developments aim at reducing mass transfer limitations, thus residence time of molecules in the zeolite crystal. Several strategies can be found in the literature to reach this goal, all leading to an increase of the (external surface)/(internal surface) or (mesoporous surface)/(microporous surface) ratios: i) obtaining nanocrystals of zeolite (several tens of nanometers),[19-20] or even embryonic zeolites,[21-22] ii) preparing hierarchical zeolites, by introducing meso(macro)porosity in the microporous crystals,[23-25] or by preparing hollow zeolite structures,[26] iii) obtaining nanosheets of zeolite (thickness: less than 10 nm), delaminated and 2D zeolites.[27-29] Thus, advanced knowledge of the environment of surface sites at the external surface is required.

ZSM-5 (Zeolite Socony Mobil-5) is a zeolite that was discovered and multi-patented by Mobil Oil Corporation in 1969.[30-32] It is a very well-known and used catalyst in the petrochemical industry.[4] The structure type of ZSM-5 is MFI,[33] also corresponding to the silicalite-1 zeolite.[34] Besides its industrial impact, this system is used as a prototype to investigate crystal growth mechanisms.[35] A large range of crystal sizes (from a few nm to several hundreds of μm) and Si/Al ratio (currently from 8[36] to infinity in the case of silicalite-1[34]) are accessible with the same structure type. For all these reasons, we will focus on this zeolite type in the following.

The MFI structure (Figure 1-a) is composed of two 10-membered-rings (MR) interconnected channel systems, a sinusoidal and a straight one along the directions of the a and b axes respectively.[13] MFI exhibits a monoclinic structure, undergoing a phase transition toward an orthorhombic symmetry (Pnma), depending on the temperature (orthorhombic above ~330 K for silicalite-1), the Si/Al ratio (the transition temperature decreases as the Al content increases), and the presence of adsorbed molecules in the pores.[37-39]

A large set of experimental investigations has been devoted to identify the exposed surface orientations on silicalite-1 and ZSM-5, which is complex due to the existence of intergrowth phenomena that lead to poly-crystalline particles. The morphology of the crystals appears to strongly depend on the crystal size, the synthesis procedure and the choice of the structure directing agent (SDA). The formation of nanoslabs with dominant (100) expositions was observed in the very first stage of silicalite-1 crystallization.[40] A formation mechanism was proposed for these nanoslabs, as a result of a combination of ^{29}Si NMR, X-Ray Scattering and gel permeation chromatography.[41] Clathrate-like silicate units, where the SDA (tetrapropyl-ammonium hydroxide, TPAOH) is hosted in a silica matrix forming the intersection of the zeolite, were proposed.[21] In particular, a Si_{33} species (Figure 1-b and c) was proposed,[41] being an elementary portion of the straight channel, which – assembled along the b direction – makes this channel grow, and thus the (100) orientation develops. Such proposal was later debated,[42-44] due to the multi-step nature of the formation mechanism of zeolites,[45] making the level of self-organization of the systems strongly dependent on many operating parameters. More recent investigations confirmed that the Si_{33} precursor is relevant to explain part of the crystal growth.[46]

Monocrystalline MFI nano-crystals in the range of 100-200 nm could be obtained,[19,44,47-49] where the smaller ones may dispose a rounded shape preventing the identification of a well-defined surface orientation,[19,44,47] while the larger nanocrystals may have rather well-defined facets, which were, however, not indexed.[48-49] The parallelepiped shape of some of the nanocrystals suggests the existence of (100), (010) and (001) orientations, whereas the hexagonal morphology of others could be compatible with the additional presence of (101) cuts. A clear proof of the monocrystalline nature of some silicalite-1 and ZSM-5 nanocrystals (50-200 nm) was given recently.[49]

At more advanced growth regimes,[50] seeds evolve into rounded-boats crystals, themselves giving rise to coffin-shaped crystals. Rounded-boat crystals were found to be monocrystalline with dominant (010) facets, and rectangular lateral (100) facets.[50-51] (Figure 1-d) In contrast, the complexity of the intergrowth structures of the coffin-shaped crystals was inferred from X-Ray diffraction in the 80's.[52] Since then, several sets of models have been proposed, based on optical, electronic and atomic force microscopy, X-Ray and electron diffraction.[52-56] These models invoked the presence or absence of 90° intergrowth, of MEL (Mobil Eleven)-type defects, and various numbers of components for the coffin-shaped crystals. The nature of the exposed orientations thus has been subjected to debate. About 10 years ago, a consensus was obtained thanks to the use of a set of characterization techniques, in particular, confocal fluorescence microscopy with various fluorescent probes, Scanning Electron Microscopy and electron diffraction after ion-beam milling.[51,57-59]

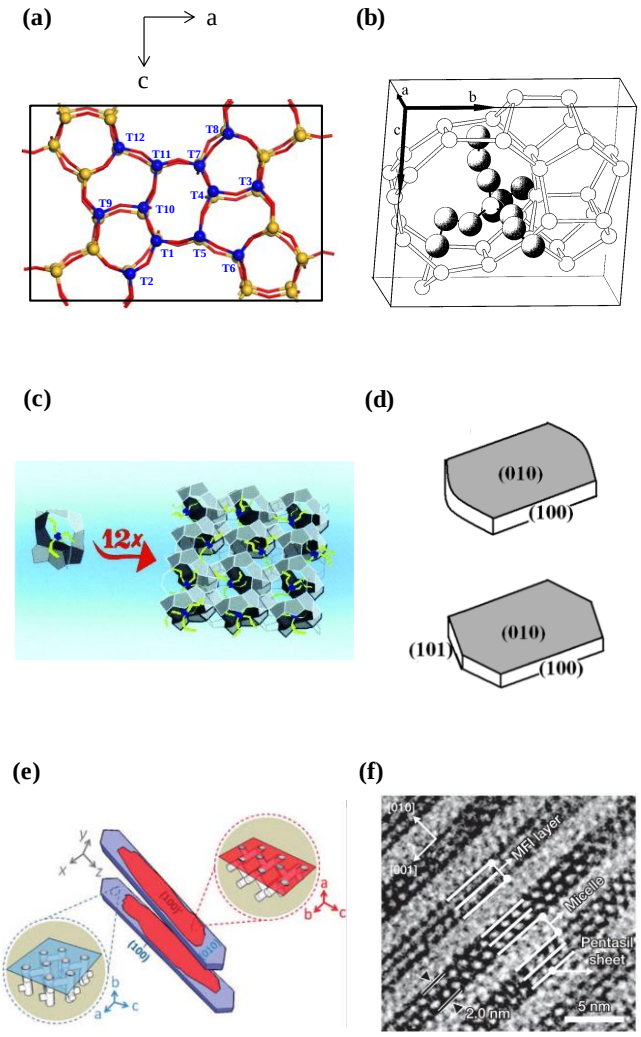

Figure 1. (a) Conventional crystalline cell of ZSM-5,the positions of oxygen atoms are represented in red, the positions of the silica are in yellow. The blue atoms represent the 12 non-equivalent positions of silicon atoms named from T1 to T12, (b) Si_{33} entity identified as the precursor of MFI nanoslabs surrounding TPAOH as SDA. Reproduced with permission from Reference [41]. Copyright 1999, American Chemical Society. (c) Formation of nanoslabs by the assembly of the Si_{33} elementary units. Reproduced with permission from Reference [40]. Copyright 2001, Wiley. (d) Schematic representation of rounded-boat (top) and coffin-shaped (bottom) crystals. Reproduced with permission from Reference [60]. Copyright 2013, The Royal Society of Chemistry. (e) Relationship between the crystallographic abc-axes and the morphological xyz-axes for coffin shaped crystals. Reproduced with permission from Reference [59]. Copyright 2008, American Chemical Society. (f) TEM of MFI nano-sheets. Reproduced with permission from Reference [28]. Copyright 2009, Nature.

These studies demonstrated the existence of several kinds of crystals, but with a common feature, that is a 90° rotation of the sub-units exposed on the "(010)" facets. These intergrowths make the (100) surface (intersecting the sinusoidal pores) largely exposed on all lateral faces of the polycrystalline crystals (Figure 1-e). Only perfectly monocrystalline coffins expose both the (100) and (010) orientations.[51] Tips of the coffins mainly expose (101) and (10-1) surface orientations.[60] Octagonal variants of the coffin shape crystals exhibit (001) and (011) orientations at their tip.[60] HRTEM (High-Resolution Transmission Electron Microscopy) was also performed on silicalite-1 crystals,[61] where (100) and (101) surface terminations have clearly been observed. Unambiguously, the (010) orientation (perpendicular to the straight channels) appears to be exposed on MFI nano-sheets[28,62] on Self-Pillared nano-sheets,[63] and on thin films grown from nano-sheets (Figure 1-f).[64-65] In some studies, seeds were employed to grow the sheets, the (010) orientation of the sheets growing aligned with the (100) plane of the seeds,[65] revealing an orthogonal rotational intergrowth relationship between the two objects.

The respective stability of these many surface orientation is however unknown, and the structure of the surface sites is supposed to be equivalent to that of the bulk crystal (bridging Si-(OH)-Al groups), but with improved accessibility. The nature and stability of the active sites at these different external surface orientations need to be unraveled. To address these key-questions, several studies

based on theoretical calculations have been undertaken. Car-Parinello molecular dynamics simulations have been reported for (010) nanosheets silicalite-1 models, revealing a significant stability of the atomic arrangement at the surface.[62] Hernandez-Tamargo *et al.* proposed the first density functional theory (DFT) detailed investigation of bridging OH groups located at the (010) surface, in the vicinity of silanols terminating the surface, but they excluded the possible formation of other types of groups.[66] Other DFT studies with different purposes were undertaken for this surface orientation.[67-70] The (001) surface was chosen to build a cluster model by Duca *et al*.[71-72] To the best of our knowledge, the most relevant (100) surface was only modeled once,[67] with small slabs saturated by Si-H groups at the bottom.

In the present work, we propose a general DFT investigation of the stability of the three dominant orientations for silicalite-1 and ZSM-5 crystals and nano-sheets: consistent models are constructed for the (100), (010) and (101) surface orientations, with an in-depth analysis of the influence of the nature of the terminating structures (varied here by changing the height of the cleavage of the bulk structure) on the thermodynamic stability. For technical reasons, the surface models are constructed by cleaving the bulk structure. Although such a process does not faithfully represent the experimental conditions, with growth mechanisms in solution at non-neutral pH and in the presence of the SDA, we manage to make a link between the simulated structures and some building blocks invoked experimentally, for all surface orientations. The consequences of the exchange of silicon by aluminum and their positions will be discussed with respect to the surface stability and the chemical nature of surface species (Si-OH, Si-OH-Al, Al-OH but more importantly Al-$(H_2O)(OH)_n$ with n=0-2) have been systematically quantified in comparison with that of bulk Si_{IV}-OH-Al_{IV} groups as a function of temperature and partial water pressure to investigate as well their hydration/dehydration properties. General rules connecting the thermal stability of surface sites and the local topology will be discussed in relation to the expected equilibrium morphologies helping to unravel the much debated question[73-77] on the framework Lewis acid sites in zeolites.

2. COMPUTATIONAL DETAILS

Periodic DFT calculations were performed with the PBE (Perdew, Burke, and Ernzerhof) exchange-correlation functional[78] as implemented in VASP 5.4.1.[79-80] The projected augmented wave (PAW) method[81] was used to describe the core-electron interactions, and the plane wave basis set was limited to a kinetic cutoff energy of 400-800 eV (depending on the kind of calculation performed, see below). A density-dependent dispersion correction, dDsC,[82] was applied. The convergence criterion for the electronic self-consistent field relaxation was fixed at 10^{-5} eV. Even for nonsymmetric slabs, no dipolar correction was applied to remove the spurious interactions in the direction perpendicular to the surface, as it has a minor impact on the electronic energy (less than 2.10^{-3} eV, see Supporting Information SI). All calculations were performed at the gamma point. Full geometry optimizations were performed using the implemented conjugate-gradient algorithm, with a convergence criterion on forces of 0.02 eV.$Å^{-1}$.

We considered the orthorhombic cell of MFI for the calculations, as it is experimentally the most stable one after thermal treatment. The bulk cell parameters and initial ionic positions were obtained from the International Zeolite Association database[13] and then reoptimized in the purely siliceous form with an increased energy cutoff of 800 eV. The final values are (almost orthorhombic α=89.99°, β=90.00°, γ=90.00°): a=19.901 Å, b=20.009 Å and c=13.364 Å, in good agreement with the experimental values[83-84] (orthorhombic: a=20.07±0.01 Å, b=19.92±0.01 Å and c=13.42±0.01 Å). These values were then kept constant throughout the study. The bulk configuration exhibits 12 non-equivalent T sites in the structure (Figure 1-a). The alumination of the bulk structure was modeled by the replacement of one silicon by an aluminum atom. A proton was added as a compensation cation on one of the neighboring oxygen of the aluminum, which induced four possibilities of bridging OH group as Al-(OH)-Si for one aluminum position. The silicic structure was cleaved along the (100), (010) or (101) surface orientations, to mimic the relevant surface orientations identified experimentally (see introduction). For each investigated cleavage direction, a set of cleavage heights was investigated as illustrated in Supporting Information SI. The thickness of the slab was initially set at two bulk units, which appeared to provide satisfactory convergence of structural properties (Supporting Information SII). The wish for simulating a symmetric slab led us in some cases to slightly deviate from this thickness (see Supporting Information SI). A 25 Å vacuum layer was added on top of the surfaces. The dimensions of the cells were 60.83×20.01×13.36 $Å^3$, 19.90×60.77×13.36 $Å^3$ and 23.97×20.01×50.17 $Å^3$ for the (100), (010) and (101) directions, respectively. Finally, the surface was saturated with OH groups, hydrogen atoms were added to monocoordinated O atoms and OH moieties saturated Si_{III}/Si_{II}/Si_I atoms. The total numbers of atoms are in the 516-642, 528-648 and 414-678 intervals for respectively the (100), (010) and (101) surface models.

The alumination energy $\Delta_r U_{al}$ is calculated with Equation 1 using the energy of the aluminated surface (or bulk) U_{slab_Al}, the energy of the surface (or the bulk) without aluminum U_{slab} and the energies $U_{Al(OH)_3H_2O}$ and $U_{Si(OH)_4}$ of the usual tetrahedral components of zeolites respectively $Al(OH)_3H_2O$ and $Si(OH)_4$. The energy of these latter two species has been calculated in a cubic cell of 30 Å side lengths.

$$\Delta_r U_{al} = (U_{slab\_Al} + U_{Si(OH)_4} - U_{slab} - U_{Al(OH)_3H_2O}) \quad \text{Eq. (1)}$$

The choice of the references is rather arbitrary, other choices could have been made with other Al/Si components. The goal of the introduction of the alumination energy is to report a straightfoward comparison of the stability of various aluminated slabs, instead of total energies.

The thermodynamic stabilities of the surfaces are determined by calculating the temperature and pressure dependent surface free energy γ_{surf}.[85] It was calculated through the formation reaction of the hydrated zeolite surface relatively to the zeolite bulk and gaseous water, as indicated by Equation 2.

$$\gamma_{surf}(T, P_{H_2O}) = \frac{1}{2A}\left(G_{surf}(T, P_{H_2O}) - N_{H_2O}G_{H_2O}(T, P_{H_2O}) - N_{Al}G_{zeo\_AlH\_bulk} - N_{SiO_2}G_{\text{zeo\_Si\_bulk}}\right) \quad \text{Eq. (2)}$$

where G_{surf}, G_{H2O}, $G_{zeo\_Al\_bulk}$ and $G_{zeo\_Si\_bulk}$ are respectively the Gibbs Free energy of the surface (which depends on the number of Si and O in the zeolite structure), the Gibbs free energy of water, the Gibbs free energy of one aluminated site in the zeolite bulk and the average Gibbs free energy of one SiO_2 units of the bulk zeolite. The vibrational contributions to the Gibbs Free energy in the bulk and surface systems are considered to be equal. Therefore, we only considered their electronic energies. N_{H2O}, N_{Al} and N_{SiO2} are respectively the number of water molecules adsorbed on the surface, the number of Al in the cell and the number of SiO_2 units in the zeolite surface model. γ_{surf} is normalized to the energy per unit area by dividing by the surface area *A*. The equilibrium morphologies were built thanks to the Morphology module of Materials Studio (Dassault Systèmes).

Hydration/dehydration reactions were simulated on one surface on the investigated slabs. Hydration Free energies were determined by evaluating the vibrational partition function of water,[86] here considered as an ideal gas. The vibrational partition function of the surface OH groups was considered as unchanged with respect to that of water, for the sake of calculation resources. The same method was applied to evaluate the adsorption energies and free energies for the adsorption of pyridine. For a limited number of cases mentioned in the following, we have explicitly evaluated the vibration free energy for condensed phases, thanks to finite difference frequency calculations, with a displacement of ±0.005 Å for the atoms allowed to vibrate (all atoms of the silicic bulk cell, half of the slab for the silicic hydroxylated surfaces, the aluminum atoms and their first, second, third and fourth neighbors for aluminated surfaces).

3. STABILITY RANKING OF SILICALITE-1 SURFACES: THE BULK CLEAVAGE APPROACH

A large set of surface models was constructed according to the method described in section 2. They differ in their surface orientation and cleavage height, which in turn results in various H_2O (in the form of Si-OH pairs) coverages: from 1.50 to 4.51 $H_2O.nm^{-2}$. The surface energies calculated at 0 K are all presented in Table S1. Consistently with previous simulations of the external surface of zeolite Beta[87] and with that of hydroxylated quartz surfaces,[88] the energies are very low and have a first-order dependence on the hydroxylation level (Figure S2), even though the local arrangement of the OH groups also influences the stability. Taking into account the effect of temperature and water partial pressure on the thermodynamic stability of the surfaces, phase diagrams have been built including surfaces that do not appear in the final diagrams (Figure 2, and Supporting Information SIII). In Supporting information SIII.3, we also report an estimation of the variation of the frontier between two cleavages, depending on the method that is used for the estimation of the vibration of condensed phase (either calculating it explicitly, or by assuming that it compensates between the various forms of water – gas phase, adsorbed- and silica –bulk, slab). At a typical water pressure of 10^{-4} bar, the frontier appears at a temperature lower by 29 K, which does not affect the conclusions drawn in the following.

For each surface orientation, above 300 K, the stability diagram is dominated by a single cleavage height, which in all cases leads to the exposition of a minimal number of Si-OH groups at the surface (θ_{H2O} = 1.50 nm^{-2} for the (100) and (010) surfaces and 1.88 nm^{-2} for the (101) surface). This means that from a thermodynamic point of view, conserving most siloxane bridges, also present in the bulk, is a strong thermodynamic driving force, giving a substance to the minimum cut hypothesis made previously,[89] although this does not appear from the consideration of surface energies at 0 K. For the (100) surface, the preferred model exhibits a straight pore cut at the half as represented in Figure 2-a (and Figure S2), exhibiting pairs of vicinal and non-vicinal silanol groups, connected one to another by hydrogen bonds. The two other models exhibiting a (narrow) stability domain in Figure 2-a are cut at the border of the straight channel (model n°6) or make the straight channel flush (model n°10) (Figure S2). In these cases, germinal silanols are exposed and groups of three silanols are connected to the same Si.

For the (010) orientation, the preferred cleavage corresponds to height n° 2, with full pentasil layers (contrary to the other cleavage height, which cut a part of the pentasil layer), consistently with previous computational works[66] and with experimental knowledge of nanosheets.[28,90]

Finally, for the (101) orientation, the termination of the most stable cleavage 6 exhibits terminal and germinal silanols. It also corresponds to the case, where all the units connected to the straight channels are uncut.

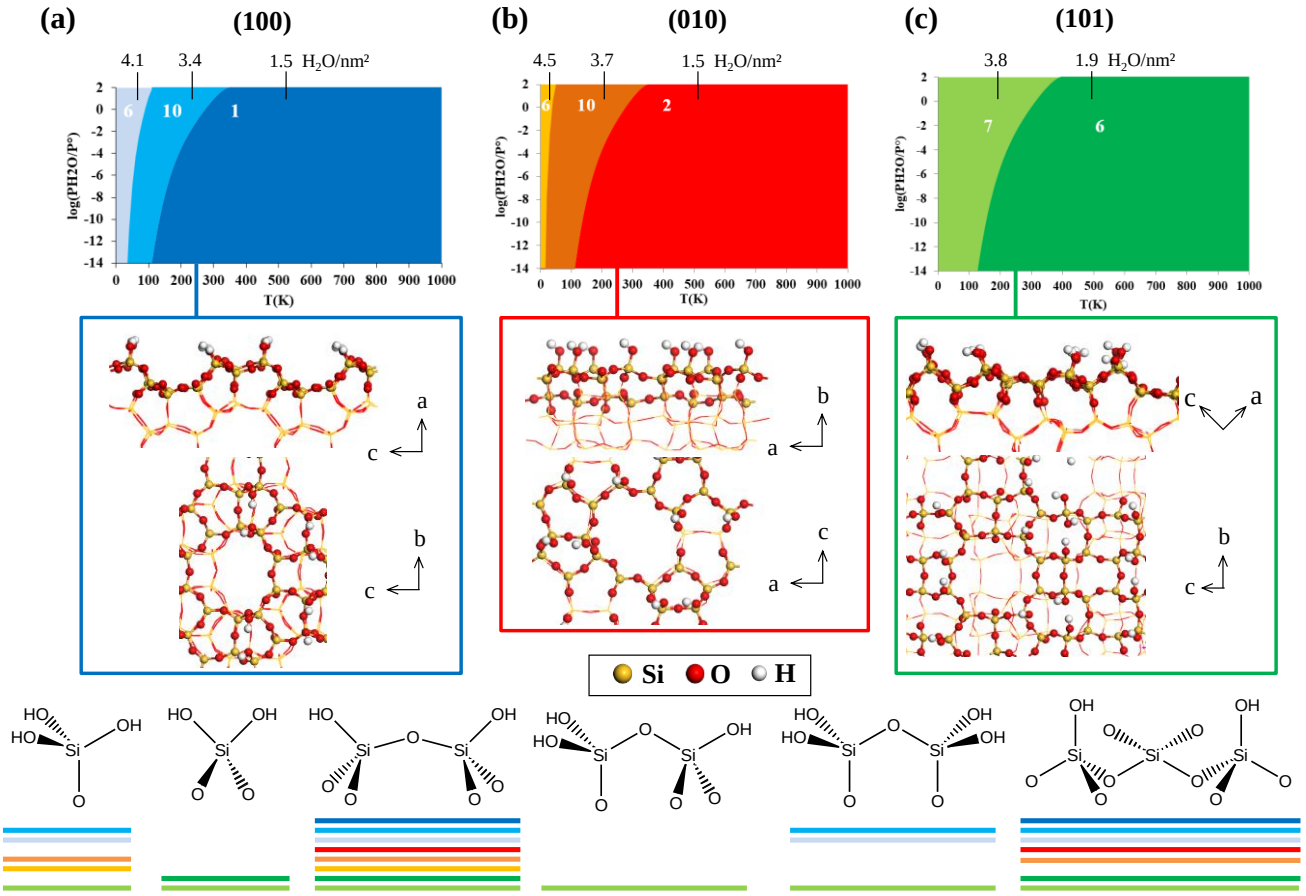

Figure 2. Stability diagrams (top) and most surface models (side and top views) for the siliceous (a) (100), (b) (010) and (c) (101) surface orientations. The numbers in the diagrams correspond to the thermodynamically most stable heights for the cleavages (see Supporting Information SI for details). The typical surface groups that are present at the surface cleavage are depicted at the bottom of the figure; they are underlined with the colors used in the stability diagrams to show under which conditions these groups are present.

Next, we compare the stabilities of the various surface orientations with each other (Table 1 and Supporting Information SIII.2). At 400 K (a typical temperature for zeolite synthesis[35,45]) and P_{H2O} = 1 bar, the surface free energy of the (100) surface is slightly lower (12.7 mJ/m²) than that of the (010) surface (13.1 mJ/m²). The (101) surface is less stable than the two other ones (14.2 mJ/m²). Following the Gibbs-Curie-Wulff law,[91-92] the equilibrium morphology corresponds to the one depicted in Figures 3-a and b.
An hexagonal prism is predicted, but shorter than the experimental coffins along the c direction. The projections show that we should expect rectangular and almost regular hexagonal shapes in microscopy, which compare very well with some studies dealing with well-defined silicalite-1 nanocrystals.[48-49,93] Gruene *et al.*[49] measured the dimensions of their silicalite-1 monocrystals. The hexagonal projection of the model exhibits a ratio of the longest over shortest dimension of 1.29d/0.96d = 1.34 (d being the height of the coffin, Figure 3-a), in very good agreement with the experimental measurement value of 1.20.[49] (Supporting Information SIV). However, TEM also shows that the height /width ratio of the particles (125 nm / 210 nm = 0.60) is smaller than the one we predict by our thermodynamic approach (d/0.96d = 1.04), suggesting that the growth of (100) facets is somewhat slower than the one of the (010) in this range of size.

Table 1. Surface energies γ_{surf} (mJ.m^{-2}) at 400K and P(H_2O) = 1 bar, of purely silicic cleavages (CLV) for the (100), (010) and (101) surface orientations and the same cleavages for similar aluminum contents.

		(100) CLV1	(010) CLV2	(101) CLV6	(101) CLV9
Purely silicic	γ_{surf}	12.7	13.1	14.2	17.4
Aluminated surface	Al.nm^{-2}	0.37	0.38	0.41	0.41
	γ_{surf}	11.0	11.5	12.8	14.7

4. STABILITY RANKING OF SILICALITE-1 SURFACES: THE PRECURSOR GROWTH APPROACH

While the approach detailed in section 3 essentially considers thermodynamic conditions, the exposed surfaces are also dictated by crystal growth conditions in solution. A Si_{33} precursor structure has been proposed from a set of experiments by Kirschhock *et al.*[41] in the presence of TPA as SDA (Figure 1-b and c). The analyses of the terminations that can be obtained from this Si_{33} precursor (Figure 4-a), reveal a strong similarity with the termination modeled upon cleavage of the crystal structure. Following the mechanism proposed in Figure 1-c,[40] the (100) surface orientation is developed in the first stages of the crystal growth. As the Si_{33} species is not symmetric, two surfaces are formed, which appeared to be similar to cleavages n°1 and 2 (Figure 4-b, see also Supporting information SV). Cleavage n°1 is the dominant one from the thermodynamic cleavage approach (Figure 2-a), meaning that in this case, thermodynamic and kinetic driving forces for crystal growth are converging. Cleavage n°2 is thermodynamically significantly less stable than cleavage n°1 (Supporting Information SIII.1). We shall next consider the stacking of two nanoslabs one with the other to make the crystal grow in the *a* direction (one of the possibilities suggested by ref. [94]). Two scenarios may be followed to form of a double nanoslab: exclusively exposing cleavage n°1 (type 1, Figure 4-c) or exclusively exposing n°2 (type 2, Figure 4-d) Cleavage n°1 being the more stable, type 1 thus becomes the most favorable one. On the other hand, if an odd number of nanoslabs is staked along the a direction during the crystal growth, both surfaces will be exposed.

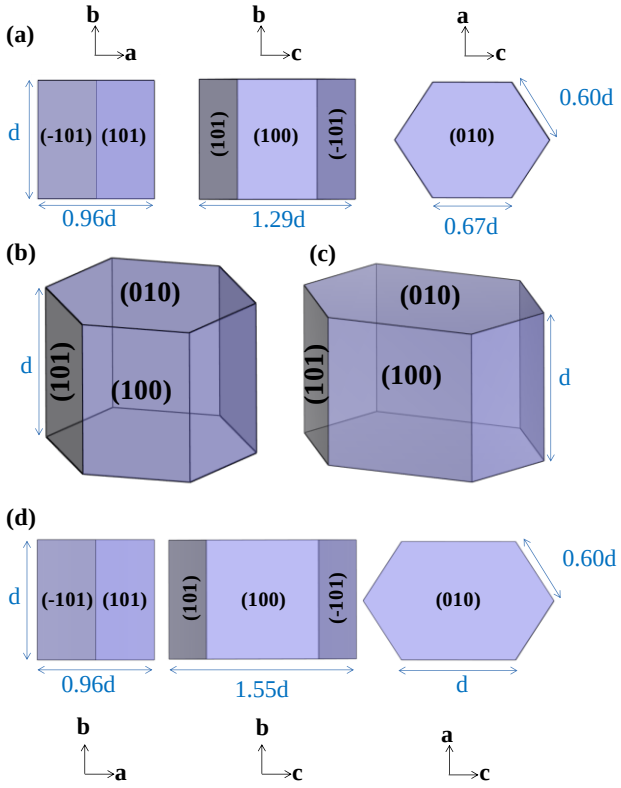

Figure 3. Equilibrium morphology of silicalite-1 and ZSM-5 crystals predicted by a Gibbs-Curie-Wulff approach, from the surface free energies calculated at 400 K and 1 bar, considering the (100), (010) and (101) orientations. (a) and (b): most stable morphology predicted by the bulk cleavage approach, (c) and (d): approximation of the morphology predicted upon construction of the surface models with the Si_{33} precursor building block approach (see also Figure 4). (a) and (d) are projections along specific axes.

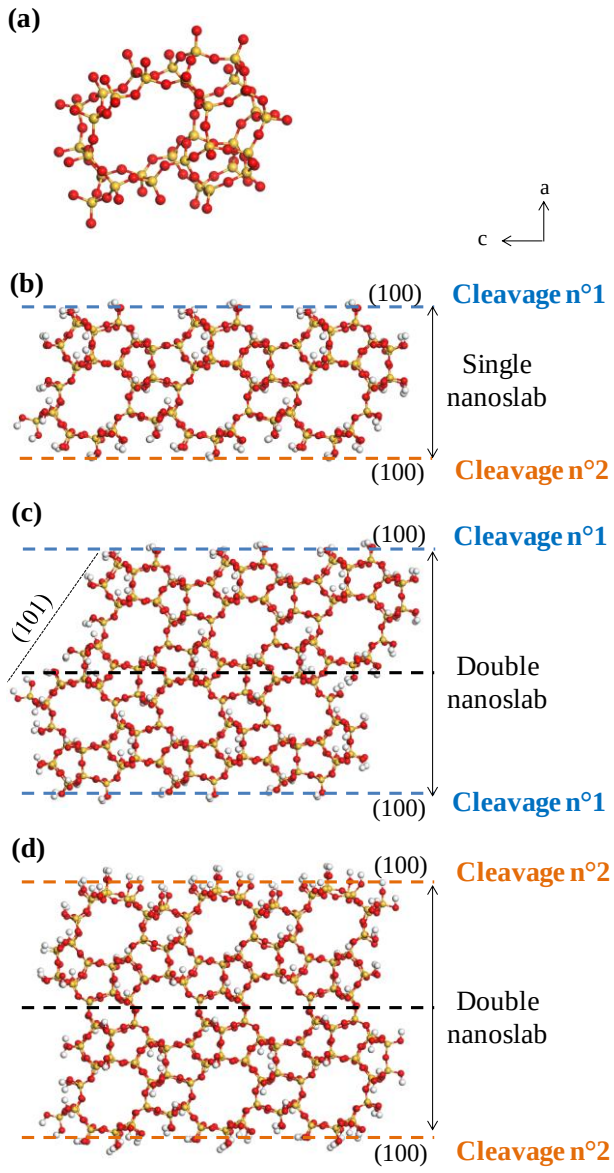

Figure 4. (a) Si_{33} precursor species constructed in the spirit of Kirshhock *et al*.[41] from the optimized bulk MFI structure; (b) lateral view of the structure of a nanoslab, exhibiting (100) surfaces, constructed in the spirit of ref. 40. The nature of the equivalent cleavages along the (100) surface is depicted. Stacking of two nanoslabs along the a axis, making cleavage n°1 (c) or n°2 (d) being solely exposed. Note that the structure of the isolated nanoslabs was not relaxed. Same color code as Figure 2.

Note that as by construction we find a perfect correspondence between the surfaces exposed by this growth approach and the systems obtained by the cleavage approach (section 3), the energies of the systems obtained by the growth approach were not evaluated.

A similar construction approach for the (010) and (101) orientations with the Si_{33} precursor was undertaken (Supporting information SV). According to Figures 4-c and d the (010) orientation is actually one of the surfaces that grows most importantly, when constructing double nanoslabs by extension along the *a* axis. From this construction method, cleavage n° 2 of the (010) orientation appears on both sides, in full agreement with the bulk cleavage approach (Figure 2-b), and with previous structural considerations.[95] Regarding the (101) orientation, construction with the Si_{33} precursors leads to a surface that is very similar (but not strictly identical) to cleavage n° 9, obtained using the bulk cleavage approach. At 400 K and P_{H2O} = 1 bar, this surface cleavage is less stable (γ_{surf} = 17.4 mJ/m²) than cleavage n°6 (14.2 mJ/m²). Thus, the equilibrium morphology predicted by such a crystal growth approach does not differ much from the one deduced from the bulk cleavage approach, as the (100) and (010) models do not change. The change

in the (101) cleavage to be considered leads to a destabilization of the latter surface with respect to the (100) and the (010) ones, thus resulting in longer coffin-like geometries (Figure 3-c and d).

In the following, we consider the introduction of aluminum in the ZSM-5 models. We start with the silicalite-1 models established in sections 3 and 4, where in the first place we investigate the cleavages n°1 and 2 for respectively the (100) and (010) surfaces, as result of their large thermodynamic stability domain and their relevance in the crystal growth with the Si_{33} building block approach. However, the other models are not excluded for further investigations, as they may also be relevant in kinetically controlled growth conditions,[96-97] where a diversity of precursors may play a role.[44]

5. STABILITY OF ALUMINUM-CONTAINING SURFACES: DIVERSITY OF SURFACE SITES

5.1. Preliminary investigation: thermodynamic preference of aluminum for bulk framework sites

The alumination of the bulk structure has been simulated by replacing one silicon by an aluminum atom, in one of the T site positions. To compensate the charge, a proton was added on one of the neighboring oxygen atoms of the aluminum, which give rise to four possibilities of Al-(OH)-Si bridging OH groups for one aluminum position. The alumination energies $\Delta_r U_{al}$ were calculated using Equation 1 and are reported in Figure 5. The detailed value of each point is presented in Supporting Information SVI.1. The lower (more negative) the value, the more stable the site. $\Delta_r U_{al}$ values range between -8 and -44 kJ.mol^{-1}, which is similar to the previous results for zeolite beta[87] (domain between -45 and 5 kJ.mol^{-1}). The domains also correspond to the 50-60 kJ.mol^{-1} range previously found for many zeolites,[98-99] including bulk ZSM-5,[67,100-103] mordenite[104-105] and EU-1,[106] to cite a few.

On the basis of thermodynamic stability, our calculations indicate that the T3 sites are the most likely ones to be occupied by Al, in close competition with T8 (Supporting Information SVI). However, not all computational investigations agree on this point,[67,101,107] suggesting that the difference in stability of these sites is not sufficiently pronounced, to draw conclusions and that other (kinetic) factors may also play an important role. Similar to other studies however,[101,107-108] some sites located at the intersection of both kinds of channels are the most stable one, despite being also the one that are easiest dislodged upon steaming.[109-111] Furthermore, the position of the Al atom can experimentally be tuned by changing the synthesis conditions.[111-114] Therefore, considering all possible positions is required to get a complete view of the stability of the systems.

5.2. Nature and stability of surface alumination sites

Whereas bridging OH groups are the only possibility in the bulk, the alumination of silicon atoms located at the surface (Si-OH) generates new sites. The structure and stability of these sites were sampled on several cleavages of the surface orientations considered, and are depicted in Figure 5. Details are given in Supporting Information SVI.2. Generally speaking, the reaction energy interval of surface species is larger than in the bulk, suggesting the importance of numerous local effects playing a role on the preferential location of {Al,H} pairs. For each family of surface groups, the configurations leading to the most negative alumination energies are those where the introduced proton becomes a hydrogen bond donor towards a pre-existing Si-OH group, explaining why the most negative alumination energies are found for silanol-rich surfaces. We did not find a direct relation between the stability of the corresponding bulk site (Table S13) and $\Delta_r U_{al}$.

"Classical" bridging OH groups appear to be distributed according to a similar alumination energy range at the surface and in the bulk. At the surface, a larger variety of bridging OH groups is moreover obtained, where an additional terminal OH group is connected to the Al and/or Si atom. Some of these groups exhibit a significantly more negative alumination energy with respect to bulk bridging OH groups, resulting from the extra-hydrogen bond as mentioned above.

In the case when the aluminum is situated at the surface, i.e. it is connected to at least one surface OH oxygen, the compensation proton can also bind to the surface Al-OH groups and generate an adsorbed H_2O molecule, yielding an Al-(H_2O) species, as already has been shown for zeolite beta.[87] Some silicon atoms at the surface are linked to the bulk of the zeolite by one of two Si-O-Si bridge and are connected to three or two OH groups. The alumination of these silicon atoms generates Al-(H_2O)$(OH)_n$ species with n = 1 or 2. It appears from Figure 5 that Al-(H_2O)$(OH)_n$ species (with n = 0-2) are the most stable ones, whatever the surface orientation under consideration. The stability domains are lying in a very large range (between -140 and -30 kJ.mol^{-1}) even though the majority falls in the range between -100 and -50 kJ.mol^{-1}. For all the surface orientations, the closer the aluminated sites are to the outermost surface, the more stable they are. Note that in the previous DFT simulations of MFI surfaces, these most stable configurations were often omitted.[66-67] In some cases, they were considered as precursor states for the dehydration of the surface,[66,115] which we further investigate in section 6.

Thus, the bridging Si-OH-Al groups can exist at the pore mouth, strengthening the pore mouth catalysis concept.[17-18] But, they do not exist at the outermost surface, confirming the idea that the existence of the cavity is needed to stabilize such bridging groups.[116-117]

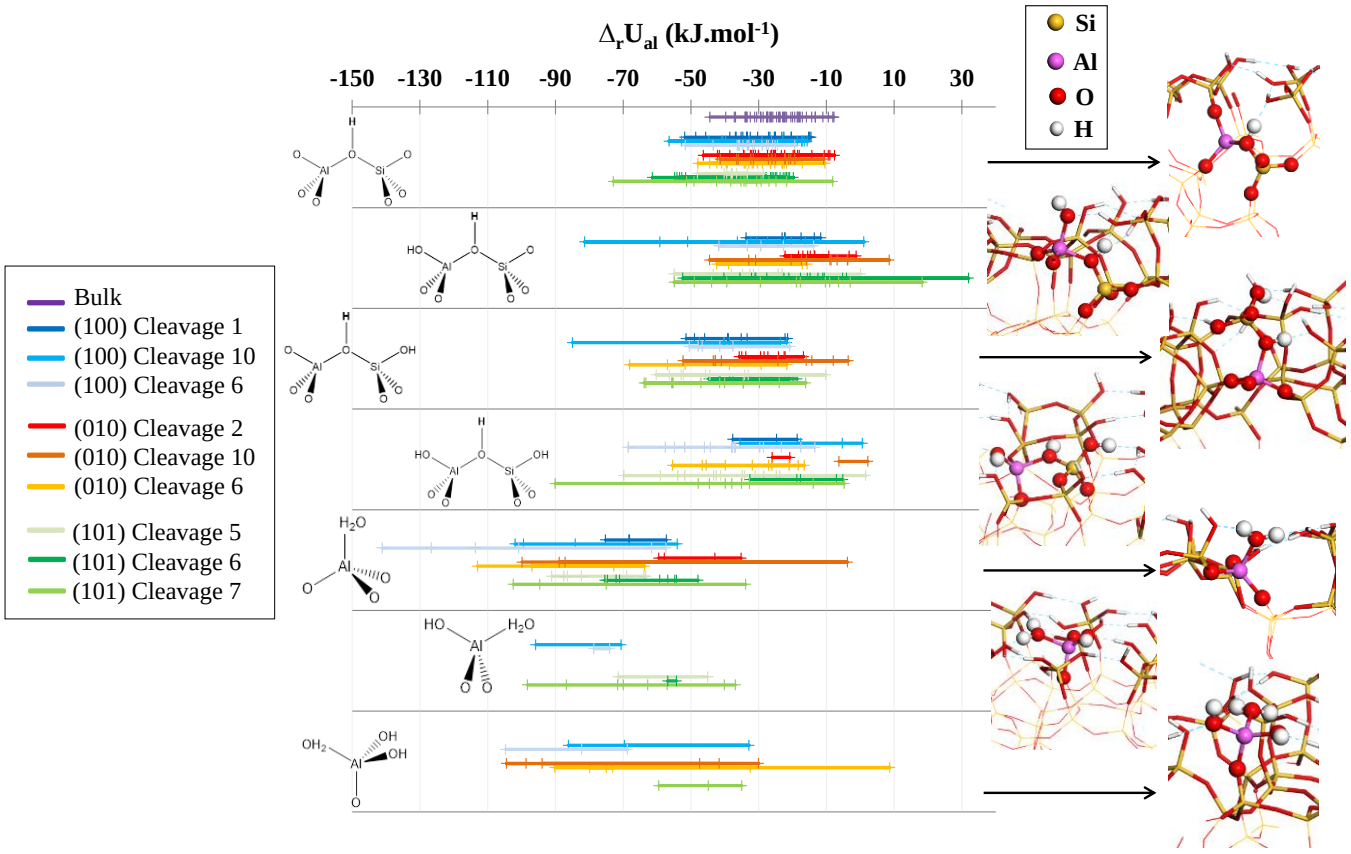

Figure 5. Alumination energy along the various considered cleavages, and in the bulk of ZSM-5, for the large variety of considered aluminated sites. On the right, the site corresponding to the lowest alumination energy for a given kind of site is shown.

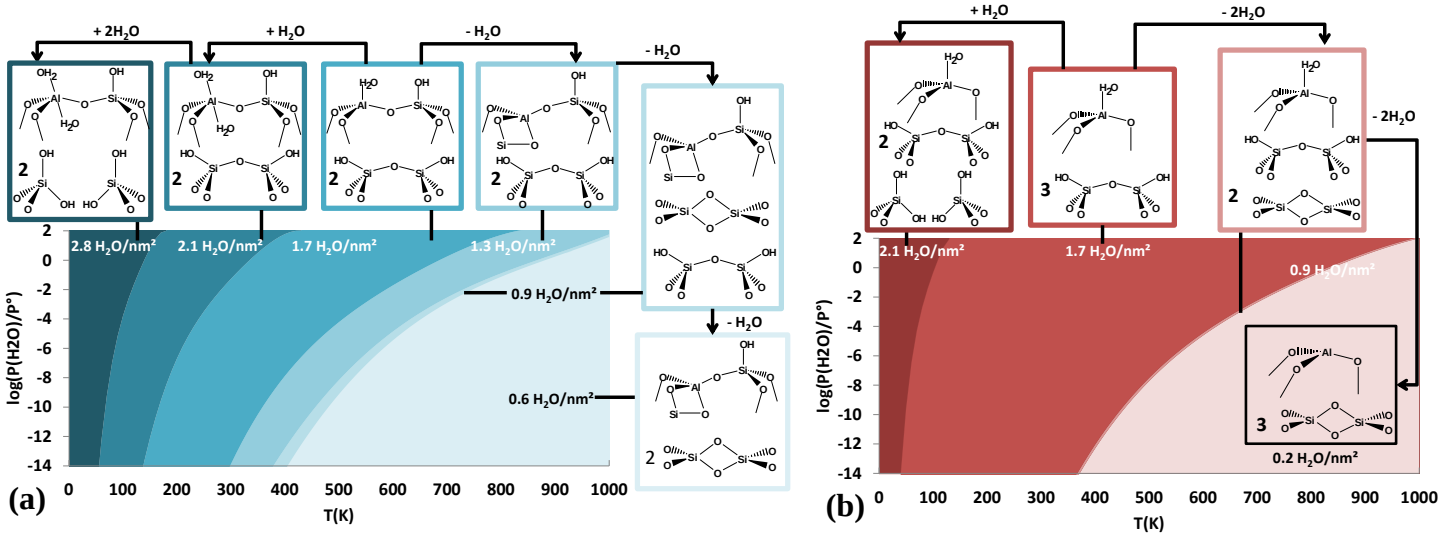

Figure 6. Surface hydration thermodynamic diagram for two types of Al-(H_2O) sites belonging to the Cleavage 1 of (100) surface of ZSM-5. (a) site n°59 and (b) site n°75. The terminology of the surface sites is given in Figure S14.

5.3. Impact of the Si/Al ratio

The influence of the Si/Al ratio on the stability of the system was investigated for cleavage 1 along the (100) surface orientation, and cleavages 6 and 9 along the (101) surface orientation. Instead of one, 4 T and 2 T sites per unit cell were substituted by Al for respectively the (100) and (101) orientations. These Al atoms were introduced at the surface, similar to what would have taken

place in the case of zoned Al distribution.[118] For the calculation of the local Si/Al ratio, we may consider the surface layer corresponding to one bulk unit. This leads to variation intervals between 23 and 95 for the (100) orientation, 43 and 102 for the (101) orientation. This is representative of most experimental investigations: the Si/Al ratio of ZSM-5 varies from 8[36] to infinity[34] (silicalite-1), with a predominance of investigations dealing with Si/Al>15. Results are reported in Table S14. In this range of Si/Al variation, the lateral interaction between the acid sites themselves is negligible. Also in the case of zoning, bulk calculations suggest that the average alumination energy may not strongly depend on the Si/Al ratio down to local values of 8.[119]

In the end, the presence of aluminum affects the stability of the surface terminations, and thanks to DFT we can quantify this effect. Whereas the alumination energy quantifies the respective stabilities of silicon *versus* aluminum sites at a given position, the equilibrium morphology is given by the nature of the most stable aluminated surface termination. For similar surface aluminum contents (0.37, 0.38 and 0.41 Al.nm^{-2} for the (100), (010) and (101) surface orientations respectively), the surface energies are the following: 11.0, 11.5, 12.8 and 14.7 mJ/m² for the (100) (cleavage 1), (010) (cleavage 2), (101) (cleavages 6 and 9) respectively (Table 1). These values lead essentially to the same equilibrium morphology as compared to silicalite (Figure 3). Experimentally, some differences were observed in some studies between silicalite and ZSM-5,[49] suggesting that kinetic limitations may take place for the growth in some directions, which depend on the Al concentration in the medium, and/or that the Al content is not the same on any surface orientation.[118]

6. THERMAL STABILITY: HYDRATION AND DEHYDRATION PROPERTIES

Considering the presence of non-dissociated water molecules at the external surface of zeolites also requires to study the thermal stability as function of temperature and partial water pressure. We therefore undertook a systematic investigation of the hydration/dehydration reactions that are likely to take place on a selection of relevant surface systems. Al-(H_2O) species at the (100) surface are first studied and compared to what we call the reference state – representing the surface obtained after cleavage, saturation by Si-OH groups and alumination as described in the previous sections. Three sites were selected: on cleavage 1, the least (Figure 6a) and the most (Figure 6b) stable Al-(H_2O) group, and the most stable site for cleavage 6 (Figure S17), which is also the most stable site simulated for all (100) investigated configurations. Several kinds of reactions give rise to stable products on the phase diagram: desorption / adsorption of water from / to Al-(H_2O) sites; hydrolysis of siloxane bridges; and condensation of silanols pairs (vicinal or not) to generate new siloxane bridges. An example of such a detailed study is provided in the Supporting Information SVII. Several configurations were studied for each hydration or dehydration levels and the most stable configurations were selected. Phase diagrams were then constructed (Figure 6 and S17), where the evolution of the surface free energy is plotted with respect to temperature and water partial pressure. Here again, the effect of the consideration of the vibrational free energies of surfaces was taken into account in a few cases, which demonstrate a moderate variation of the transition temperatures (Figure S9).

The coordination number of Al, initially modeled at 4, was shown to increase upon water adsorption to 5 as shown in Figure 6 and S17. This is in agreement with the spectroscopic data obtained by Al K-Edge XAS and ^{27}Al NMR, where the coordination number even reaches six.[75,120] In fact, we could simulate Al_{VI} species with two H_2O molecules coordinated onto the surface Al atom, whose stability appeared to be similar to that of hydrolyzed siloxane bridges, that in turn is expected to be stable below room temperature. For the three investigated cases, depending on the local environment, two typical behaviors of the aluminum sites above room temperature were encountered upon heating (Figure 6, S17 and 7):

- The water desorbs, leading to the formation on an under-coordinated Al_{III};
- In those cases where a framework oxygen atom from a siloxane bridge, is accessible below this Al_{III} atom, a new Al-O bond is formed, leading to a (distorded) Al_{IV} instead of an Al_{III}. This situation has also been encountered for the Beta zeolite.[87]

In the second case, the desorption of water from the aluminum atom represents the most favorable dehydration reaction, starting from the reference system. Conversely, for the configuration where Al remains Al_{III}, the closure of siloxane bridges takes place at lower temperature. It gives rise to 2MR rings as for cleavage 1, site n° 75 (Figure 6-b) or to form larger surface rings upon temperature increase and water desorption, like for cleavage 6, site n° 77 (Figure S17).

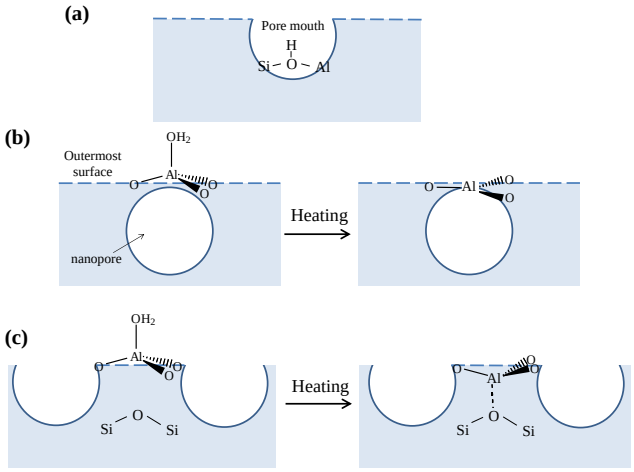

Figure 7. Dehydration of Al-(H_2O)$(OH)_n$ groups (exemplified in the case of n = 0) depending on the presence of a nanopore (b) or a siloxane bridge (c) below the Al atom, while bridging OH groups at the pore mouth (a) are stable upon dehydration.

To elucidate the general rules explaining the thermal stability of Al-(H_2O) and the nature (Al_{III} versus Al_{IV}) of the aluminium atom obtained upon dehydration, we systematically calculated and compared the desorption structures and temperature at $P(H_2O)=10^{-4}$ bar of the water molecule adsorbed on the Al atom, omitting the other kinds of dehydration reactions that also take place (e.g., the condensation of silanol groups into siloxane bridges).

Table 2. Dehydration temperature T_{des} at $P(H_2O)=10^{-4}$ bar for various Al-(H_2O) surface sites (see Figures S14 and S15 for the terminology of the sites). The shortest non covalent Al---O bond length d(Al---O) between the Al of Al-(H_2O) and the closest siloxane bridge underneath (if any), before desorption, is also given, as well as the number of hydrogen bond N_{LH} (2.5Å cutoff) between the water molecule and neighboring OH groups before desorption, and the coordination state of aluminum after water desorption.

Surface orientation	Cleavage	Site number	T_{des} (K)	d(Al---O) (Å)	N_{LH}	State of Al after desorption
(100)	1	59	507	3.003	1	Al_{IV}
		71	536	3.155	1	Al_{IV}
		87	576	3.467	1	Al_{III}
		75	622	3.330	1	Al_{III}
	6	77	684	-	2	Al_{III}
(010)	2	121	492	3.612	0	Al_{III}
		111	558	3.416	1	Al_{III}
		45	592	3.557	1	Al_{III}
		43	530	3.394	1	Al_{III}
(101)	6	19	671	3.669	1	Al_{III}
		84	538	-	1	Al_{III}
		132	640	3.822	1	Al_{III}
		37	556	3.485	1	Al_{III}
	9	8	636	3.433	2	Al_{IV}
		51	600	-	2	Al_{III}
		59	691	3.418	2	Al_{III}
		57	671	3.874	1	Al_{III}

The results are shown in Table 2. This simplified approach gives results comparable to the more detailed approach (Figure 6 and S17) for sites n°59 and 75, but a shift is seen for site n°77, showing that trends are well reproduced, but the precise desorption temperatures obtained by the simplified approach have to be considered with care. It appears that the critical distance allowing the formation of the new Al-O bond between the dehydrated Al site and the siloxane bridge underneath is between ~3.2 and ~3.4 Å. The dehydration temperature is most of the time higher when an Al_{III} is formed than when an Al_{IV} is formed, which translates into a higher reactivity of Al_{III}. But exceptions exist, in particular on the (010) orientation where Al_{III} species are formed at moderate heating temperatures (below 500K for site n°121, for example). This can be linked to the smaller number of hydrogen bonds that

stabilize the adsorbed water molecule (zero or one), due to a lower OH content (1.5 OH/nm²). Thereby, making the desorption easier than in the case of the (101) orientation at cleavage 9 (the more relevant model for the tips of the coffin-shaped crystal, according to the "crystal growth" approach), where several configurations of the water molecule are stabilized by two hydrogen bonds, thanks to a higher OH coverage (2.71 OH/nm²).

Experimentally, Al_{III} were observed or suggested by X-Ray Absorption Near Edge Structure spectroscopy and Nuclear Magnetic Resonance above 623-723 K in the case of mordenite, Beta, Ferrierite and chabazite.[73-75] Although the role of the external surface was not invoked in these works to explain the Al_{III} presence, the reactions we simulate in the present work are able to rationalize it. Also, we give here a better understanding why water desorbs easier from nanosheets, essentially represented by the (010) surface having the lowest desorption temperature, in comparison to more classical samples seen experimentally.[121]

One thus observes a strong dependence of the surface reactivity towards water, depending on the local topology of the surface sites, already for a given zeolite (here with the MFI framework), but also likely from one zeolite framework to another. In practice, many gas phase catalytic reactions using zeolites and ZSM-5 take place between 500 and 800 K.[3-5,116] Choosing a typical water pressure of 10^{-4} bar, this means that on the same sample, Al-(H_2O), dehydrated Al_{IV} and Al_{III} species will be present at the same time. Note that the bridging OH groups present at the pore mouth are expected to be thermally stable, with respect to hydration/dehydration reactions.

7. BRØNSTED AND LEWIS ACIDITY OF SURFACE SITES

Transposing the above-mentioned results in terms of acidity, it means that several families of Brønsted (BAS) and Lewis acid sites (LAS) can potentially exist under experimental conditions, depending on the operating conditions. To check this in practice, we quantified the interaction of a very popular probe molecule,[122] pyridine,[123] with the possible acid sites of the external surface (focusing here on typical sites of the (100) surface sites). Our results are reported in Tables 3 and 4, together with the adsorption geometries. For the sake of comparison, we also considered the BAS/LAS nature of one bulk site.

Consistently with previous theoretical and experimental reports,[124-125] the adsorption of pyridine at the bulk BAS leads to the proton transfer, thus forming pyridinium, stabilized by an adsorption energy of -213 kJ.mol^{-1}. Choosing a partial pressure of pyridine of 10^{-4} bar, this corresponds to a desorption temperature of pyridine of 638 K, in line with Temperature-Programmed Desorption experiments.[126] All surface sites under consideration in our computational study are able to transfer their proton to pyridine, suggesting that they are all BAS. At the bridging OH group of the pore mouth, the lowest adsorption energy found (-215 kJ.mol^{-1}) is comparable to the "bulk", proving that these sites are as acidic as the bulk sites.

Table 3. Brønsted acidity as measured by the pyridine adsorption on a selected number of protonic sites of the (100) surface (cleavage 1, see Figure S14 for the terminology of the sites). The adsorption energy $\Delta_{ads}U_{py}$ is given, as well as the corresponding dispersion ($\Delta_{disp}U_{py}$) and the non-dispersive ($\Delta_{non\_disp}U_{py}$) components of $\Delta_{ads}U_{py}$, the estimated pyridine desorption temperature $T_{des\text{-}py}$ for P(pyridine) = 10^{-4} bar, and the structure of adsorbed pyridine. Color code for the structures: oxygen: red, silicon: yellow, aluminum: purple, hydrogen: white, nitrogen: blue, carbon: grey. The same properties for the bulk site T5 are also given for comparison.

Sites (number)	Bulk	57	69	79	89	91	59	75
Nature of the reaction	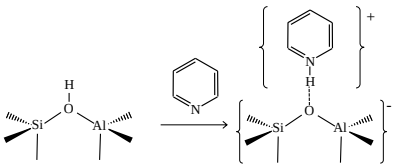						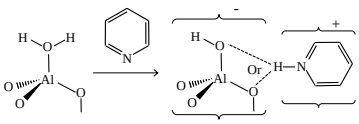	
$\Delta_{ads}U_{py}$ (kJ.mol^{-1})	-213	-180	-185	-184	-167	-215	-150	-122
$\Delta_{disp}U_{py}$ (kJ.mol^{-1})	-69	-73	-45	-88	-51	-91	-78	-47
$\Delta_{non\_disp}U_{py}$ (kJ.mol^{-1})	-144	-107	-140	-96	-116	-124	-72	-75
$T_{des\text{-}py}$ (K)	638	549	562	560	513	645	465	385

Structure of adsorbed pyridinium	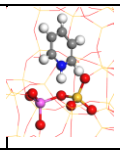	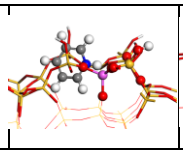	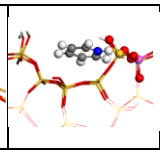	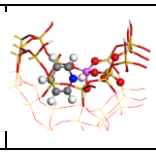	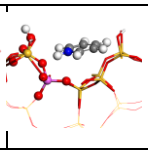	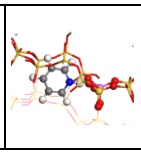	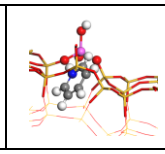	

Interestingly, the contribution of the dispersion energy to the overall adsorption energy is even more negative at the pore mouth (-91 kJ.mol^{-1}) than in the bulk (-69 kJ.mol^{-1}), showing that confinement effects play an important role at the pore mouth, resulting in a stabilization of the pyridinium ion by the sinusoidal channel. Some other sites at the pore mouth provide lower adsorption energies (between -167 and -185 kJ.mol^{-1}), corresponding to lower desorption temperatures (between 549 and 562 K), due to a slightly more external location of the pyridinium ion, or to its location in the surface straight channel only. The relatively large variations in the dispersion (between -45 and -91 kJ.mol^{-1}) and non-dispersive (-96 to -144 kJ.mol^{-1}) energy components suggest that the differences in stabilization have both van der Waals and electrostatic origins. Al-(H_2O) species exhibit lower (between -150 and -122 kJ.mol^{-1}) adsorption energies. This can be assigned again to both van der Waals and electrostatic factors. In particular, considering the most stable Al-(H_2O) group on the (100) surface orientation (n°75 in Table 3) both the dispersion and the non-dispersive terms are weaker than for the bulk or pore mouth sites. One can conclude that Al-(H_2O) sites are mild BAS. Note that these adsorption configurations of pyridinium are very similar to the one obtained after proton transfer from bridging OH groups. Pyridinium is in both cases better stabilized at the pore mouth rather than at the outermost surface. Thus, the origin of the lower acidity of Al-(H_2O) can at least in part be assigned to the higher stability of Al-(H_2O) with respect to the pore mouth bridging OH group. This is at variance with the observations made by comparing bulk zeolites and amorphous silica-alumina (ASA),[127] as in the last case the cavity effect is absent, making the lower stabilization of the protonated probe molecule the main factor to explain the milder acidity of ASA.

With respect to the Lewis acidity, we could obtain as an energy minimum a specific approach of the Al bulk site by pyridine that makes the formation of a Al-N bond possible. The approach making this possible is in anti with respect to the bridging OH group, see illustration in Table 4. This is consistent with our previous findings for water adsorption,[109-110] and with previous proposals by Busca *et al.* to explain the existence of LAS in high Si/Al faujasite samples that exhibit LAS without any EFAl.[76] After adsorption, the anti Al-OH bond is broken, forming a pseudo-bridging silanol,[128] and maintaining the coordination number of Al to four. However the adsorption energy is lower than the one for the bulk BAS, so that bulk sites will express their Brønsted acidity rather than their Lewis acidity, in line with the absence of experimental detection of LAS in the bulk of ZSM-5.[76]

A similar conclusion is reached for aluminum belonging to pore mouth bridging OH groups. Surface Al-(H_2O) also behave as poor Lewis acids (-110 kJ.mol^{-1}). In the most stable configuration found after adsorption of pyridine on the Al atom, one of the proton of the water molecule jumps onto the Si-O-Al bridge in anti to pyridine, to allow the formation of a pseudo-bridging silanol.

On the contrary, sites obtained after their dehydration (Al_{III} and Al_{IV}) interact more strongly with pyridine (with a non-dispersive term between -160 and -180 kJ.mol^{-1}). The strongest expression of Lewis acidity (-256 kJ.mol^{-1}) was found for a Al_{III} site at cleavage 6 of the (100) surface, when pyridine is able to access to the LAS by the pore underneath, with a bulk-like dispersion contribution (-83 kJ.mol^{-1}).

Table 4. Lewis acidity measured by adsorption of pyridine on selected Al sites of the (100) and (010) surfaces (see Figure S14 for the terminology of the sites). The adsorption energy $\Delta_{ads}U_{py}$ is given, as well as the corresponding dispersion ($\Delta_{disp}U_{py}$) and the non-dispersive ($\Delta_{non\_disp}U_{py}$) components of the adsorption energy, the estimated pyridine desorption temperature $T_{des\text{-}py}$ for P(pyridine) = 10^{-4} bar, and the structure of adsorbed pyridine. Color code for the structures: oxygen: red, silicon: yellow, aluminum: purple, hydrogen: white, nitrogen: blue, carbon: grey. The same properties for the bulk site T5 are also given for comparison.

Sites	Bulk	(100) cleavage 1, n°91	(100) cleavage 1, n°59, hydrated	(100) cleavage 1, n°59, dehydrated	(100) cleavage 1, n°75, dehydrated	(100) cleavage 6, n°77, dehydrated	(010) cleavage 2, n°121, dehydrated
Nature of the reaction	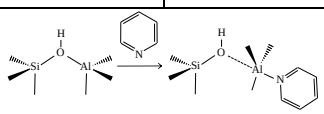 Anti approach		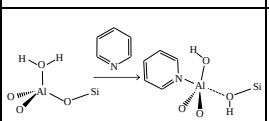	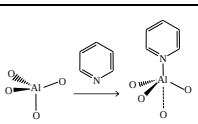	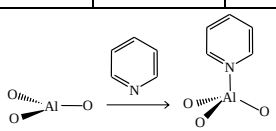		

$\Delta_{ads}U_{py}$ (kJ.mol^{-1})	-141	-122	-110	-179	-212	-256	-194
$\Delta_{disp}U_{py}$ (kJ.mol^{-1})	-81	-95	-47	-14	-33	-83	-33
$\Delta_{non\_disp}U_{py}$ (kJ.mol^{-1})	-60	-27	-63	-165	-179	-173	-161
$T_{des\text{-}py}$ (K)	440	385	350	545	638	754	589
Structure of adsorbed pyridine	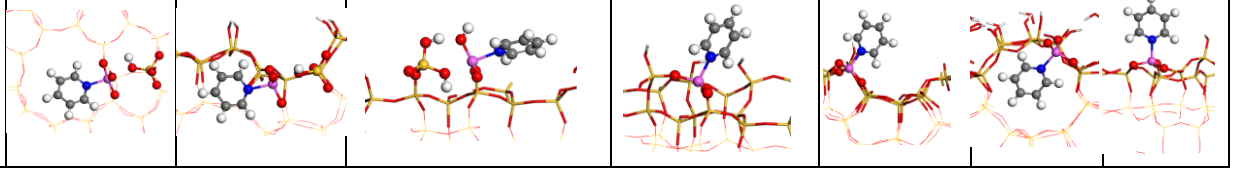						

For other cases, Al_{III} appear to be a stronger LAS (-194 to -212 kJ.mol^{-1}, desorption temperatures between 589 and 638 K) than the probed Al_{IV} (-179 kJ.mol^{-1}, 545 K), for which pyridine induces the breaking of the underneath Al_{IV}-O bond.In particular, the Al_{III} site n°121, which is easily formed upon dehydration of the (010) surface and is representative for nanosheets, exhibits a strong Lewis acidity.

Our calculations give an atomistic interpretation for the existence of BAS and LAS detected at the external surface of ZSM-5 crystals[129] and nanosheets.[90,121] In particular for nanosheets, it was found[121] that the strength of the BAS at the pore mouth is similar to that of the bulk, which is in agreement with our calculations. In ref. [121], a very intense band at 1450 cm^{-1} was observed upon pyridine adsorption on the nanosheets, which the author did not comment, but that can be assigned to a LAS. Opanasenko *et al.* also report a significant Lewis acidity of nanosheets.[130] This is in full agreement with the very easy formation of Al_{III} at the (010) surface that we calculate (Table 2), and the strong LAS character of the corresponding dehydrated sites (Table 4). This is expected to be specific for nanosheets, as for large coffin-shaped crystals, this orientation is not exposed anymore, due to intergrowths leading to the dominant (100) surface (see introduction).

Our results also explain the interconversion of BAS into LAS upon thermal treatment,[77] but without invoking severe dehydroxylation of the framework.[131] We also understand the higher number of LAS and lower number of strong BAS, observed upon pyridine adsorption for ZSM-5 as the particle size decreases,[132] or when the mesoporous volume increases,[133] even if the amount of extraframework species can also affect this feature. In the case of mordenite, it has recently been shown that the number of overcoordinated Al in wet atmosphere is directly correlated to the number of LAS (detected by pyridine adsorption) after treatment under vacuum at 723 K.[75] These sites were shown to belong to the zeolite framework and their number is directly linked to the Si/Al ratio of the zeolite. These observations can be fully rationalized by the presently proposed calculations, considering that the LAS are Al_{III} and Al_{IV} obtained after water desorption from a Al_{IV}-(H_2O) species, that can adsorb additional water molecules at the exposure of high water pressures.

Interestingly, for ordered surfaces such as the ones considered here, the structure of the sites and their acidity is different from what DFT calculations predict in the case of amorphous silica-alumina.[127-128,134-136] In particular, no pseudo-bridging OH group can be observed in the present simulation of the external surfaces of crystalline H-ZSM-5, except after adsorption of pyridine. Also, we see here that the cavity effects still play a huge role in the expression of the acidity of the external zeolite surface, whereas it is absent in the case of ASA.

This means that the optimal expression of the acidity at the pore mouth needs to control the degree of crystallinity of the external surface of the zeolite in a very cautious way. Should amorphous surface be obtained instead, dramatic consequences in terms of depletion of the acidity should be expected.

8. CONCLUSIONS

Thanks to DFT calculations, we propose a detailed model for relevant surface orientations ((100), (010) and (101)) of silicalite-1 and ZSM-5 zeolites (MFI framework), contributing to the unraveling of the nature, stability and reactivity of surface sites, as well as equilibrium morphologies of the crystallites.

A crystallography approach, consisting of the cleavage of the silicic bulk structure, is compared to a crystal growth approach, using a Si_{33} building block to elaborate surface models. Both approaches lead to very similar results in terms of preferred surfaces, except for the (101) surface, suggesting a convergence of thermodynamic and kinetic factor to describe qualitatively crystal growth for the (100) and (010) orientations. The calculated equilibrium morphologies are in qualitative agreement with microscopy pictures, although the calculated surface ratios differ to some extent, demonstrating that the experimental morphology is not fully determined

by thermodynamics, but apparently kinetic aspects need to be taken into account to further improve the description of the surface models. However, both surface models approaches describe the nature of the surface sites for nano to microcrystals, as well as nanoslabs and nanosheets.

The exchange of silicon by aluminum atoms at the surface was then examined, as well as the corresponding thermal stability of the sites, by considering the hydration and dehydration reactions, and calculating the Lewis and/or Brønsted acidity, probed by the simulation of pyridine adsorption. A diversity of surface sites in terms of nature, stability and strength has been identified thanks to this approach.

Bridging Al-OH-Si are present at the pore mouth, where the effect of the cavity is present. They are of similar or higher stability with respect to bulk sites. They are also thermally stable and exhibit similar (strong) Brønsted acidity with respect to bulk sites. They can be considered to be responsible for what is called "pore mouth catalysis". They are however not the most stable groups at the outermost surface where the effect of the cavity is absent.

At the outermost surface, the following groups prevail: Si-OH, Al-OH groups, and most importantly water adsorbed on aluminum Al-$(H_2O)(OH)_n$. They behave as milder Brønsted acid sites with respect to bridging OH groups, mainly because of their intrinsic higher stability. Whatever the starting OH group, the pyridinium cation will stabilize at the pore mouth.

However, the adsorbed water molecule is shown to desorb upon heating, revealing a surface aluminum, which behaves as a Lewis acid site. The desorption of water is calculated to occur at temperatures that strongly depend on the local topology of the surface site, and on the surface orientation. Factors that enhance the desorption of water are: i) the presence of a siloxane bridge below the surface Al atom, or ii) low OH content on the surface orientation, making the adsorbed water molecule less stable. The second factor dominates in the specific behavior of the (010) orientation, being a representative for nanosheets, thus holding easy-to-form Al_{III} ions that behave as strong Lewis acid sites. Conversely, the OH-rich (101) surface (at the tips of the coffin-shaped crystals) leads to more stable Al-(H_2O) groups, which are mild Brønsted acid sites.

These results provide a rational understanding of a large set of experimental observations from the literature, that remained so far poorly understood. They also show that in typical industrial operating conditions (between 500 and 700 K, water pressure of the order of 10^{-4} mbar), several kinds of sites co-exist: strong BAS in the pore mouth, mild BAS and LAS at the outermost surface.

These findings are likely not limited to the case of the MFI framework (some of them already appeared to be valid for the zeolite Beta), as our conclusions are mainly dictated by local topology aspects. Controlling the global topology of the network may tune the respective concentration of the different acid sites, but also the confinement effects for bulky molecules that cannot access the bulk sites. All these aspects, together with transport limitations within the framework, contribute to the final properties of the system.

Corresponding Author

* Céline Chizallet, IFP Energies nouvelles
celine.chizallet@ifpen.fr

Author Contributions

The manuscript was written through contributions of all authors. All authors have given approval to the final version of the manuscript.

Supporting Information. Variation of the cleavage height for each surface orientation; Convergence of the calculated properties as a function of the slab thickness; Surface free energies of the various surfaces; Morphology constructions and comparison with experiments; Construction of surface model from the Si_{33} precursor species; Alumination energies; Surface hydration/dehydration reactions.

This material is available free of charge via the Internet at http://pubs.acs.org.

ACKNOWLEDGMENT

This work was performed using HPC resources from GENCI (Grant A0020806134) and the ENER200 cluster at IFP Energies nouvelles.

REFERENCES

(1) Davis, M. E., Ordered Porous Materials for Emerging Applications, *Nature* **2002**, *417*, 813.

(2) Corma, A., Inorganic Solid Acids and their Use in Acid-Catalyzed Hydrocarbon Reactions, *Chem. Rev.* **1995**, *95*, 559-614.

(3) Marcilly, C. *Acido-Basic Catalysis*; Technip: Paris, 2005.

(4) Vermeiren, W.; Gilson, J. P., Impact of Zeolites on the Petroleum and Petrochemical Industry, *Topics Catal.* **2009**, *52*, 1131-1161.

(5) Vogt, E. T. C.; Weckhuysen, B. M., Fluid Catalytic Cracking: Recent Developments on the Grand Old Lady of Zeolite Catalysis, *Chem. Soc. Rev.* **2015**, *44*, 7342-7370.

(6) Deka, U.; Lezcano-Gonzalez, I.; Weckhuysen, B. M.; Beale, A. M., Local Environment and Nature of Cu Active Sites in Zeolite-Based Catalysts for the Selective Catalytic Reduction of NOx, *ACS Catal.* **2013**, *3*, 413-427.

(7) Borfecchia, E.; Beato, P.; Svelle, S.; Olsbye, U.; Lamberti, C.; Bordiga, S., Cu-CHA – A Model System for Applied Selective Redox Catalysis, *Chem. Soc. Rev.* **2018**, *47*, 8097-8133.
(8) Paolucci, C.; Khurana, I.; Parekh, A. A.; Li, S.; Shih, A. J.; Li, H.; Di Iorio, J. R.; Albarracin-Caballero, J. D.; Yezerets, A.; Miller, J. T.; Delgass, W. N.; Ribeiro, F. H.; Schneider, W. F.; Gounder, R., Dynamic Multinuclear Sites Formed by Mobilized Copper Ions in NOx Selective Catalytic Reduction, *Science* **2017**, *357*, 898-903.
(9) Ennaert, T.; Van Aelst, J.; Dijkmans, J.; De Clercq, R.; Schutyser, W.; Dusselier, M.; Verboekend, D.; Sels, B. F., Potential and Challenges of Zeolite Chemistry in the Catalytic Conversion of Biomass, *Chem. Soc. Rev.* **2016**, *45*, 584-611.
(10) Derouane, E. G.; André, J. M.; Lucas, A. A., Surface Curvature Effects in Physisorption and Catalysis by Microporous Solids and Molecular Sieves, *J. Catal.* **1988**, *110*, 58-73.
(11) Gallego, E. M.; Portilla, M. T.; Paris, C.; León-Escamilla, A.; Boronat, M.; Moliner, M.; Corma, A., "Ab initio" Synthesis of Zeolites for Preestablished Catalytic Reactions, *Science* **2017**, *355*, 1051–1054.
(12) Yarulina, I.; De Wispelaere, K.; Bailleul, S.; Goetze, J.; Radersma, M.; Abou-Hamad, E.; Vollmer, I.; Goesten, M.; Mezari, B.; Hensen, E. J. M.; Martínez-Espín, J. S.; Morten, M.; Mitchell, S.; Perez-Ramirez, J.; Olsbye, U.; Weckhuysen, B. M.; Van Speybroeck, V.; Kapteijn, F.; Gascon, J., Structure–Performance Descriptors and the Role of Lewis Acidity in the Methanol-to-Propylene Process, *Nature Chem.* **2018**, *10*, 804-812.
(13) Baerlocher, C.; McCusker, J. K., *Database of Zeolite Structures:* http://www.iza-structure.org/databases/.
(14) Uytterhoeven, J. B.; Christner, L. G.; Hall, W. K., Studies of the Hydrogen Held by Solids. VIII. The Decationated Zeolites, *J. Phys. Chem.* **1965**, *69*, 2117-2126.
(15) Haag, W. O.; Lago, R. M.; Weisz, P. B., The Active Site of Acidic Aluminosilicate Catalysts, *Nature* **1984**, *309*, 589-591.
(16) Mortier, W. J.; Sauer, J.; Lercher, J. A.; Noller, H., Bridging and Terminal Hydroxyls. A Structural Chemical and Quantum Chemical Discussion, *J. Phys. Chem.* **1984**, *88*, 905-912.
(17) Martens, J. A.; Souverijns, W.; Verrelst, W.; Parton, R.; Froment, G. F.; Jacobs, P. A., Selective Isomerization of Hydrocarbon Chains on External Surfaces of Zeolite Crystals, *Angew. Chem. Int. Ed.* **1995**, *34*, 2528-2530.
(18) Martens, G. G.; Marin, G. B.; Martens, J. A.; Jacobs, P. A.; Baron, G. V., A Fundamental Kinetic Model for Hydrocracking of C8 to C12 Alkanes on Pt/US–Y Zeolites, *J. Catal.* **2000**, *195*, 253-267.
(19) Grand, J.; Talapaneni, S. N.; Vicente, A.; Fernandez, C.; Dib, E.; Aleksandrov, H. A.; Vayssilov, G. N.; Retoux, R.; Boullay, P.; Gilson, J.-P.; Valtchev, V.; Mintova, S., One-Pot Synthesis of Silanol-Free Nanosized MFI Zeolite, *Nat. Mater.* **2017**, *16*, 1010-1015.
(20) Mintova, S.; Jaber, M.; Valtchev, V., Nanosized Microporous Crystals: Emerging Applications, *Chem. Soc. Rev.* **2015**, *44*, 7207-7233.
(21) Chang, C. D.; Bell, A. T., Studies on the Mechanism of ZSM-5 Formation, *Catal. Lett.* **1991**, *8*, 305-316.
(22) Haw, K.-G.; Gilson, J.-P.; Nesterenko, N.; Akouche, M.; El Siblani, H.; Goupil, J.-M.; Rigaud, B.; Minoux, D.; Dath, J.-P.; Valtchev, V., Supported Embryonic Zeolites and their Use to Process Bulky Molecules, *ACS Catal.* **2018**, *8*, 8199-8212.
(23) Valtchev, V.; Majano, G.; Mintova, S.; Perez-Ramirez, J., Tailored Crystalline Microporous Materials by Post-Synthesis Modification, *Chem. Soc. Rev.* **2013**, *42*, 263-290.
(24) Perez-Ramirez, J.; Christensen, C. H.; Egeblad, K.; Christensen, C. H.; Groen, J. C., Hierarchical Zeolites: Enhanced Utilisation of Microporous Crystals in Catalysis by Advances in Materials Design, *Chem. Soc. Rev.* **2008**, *37*, 2530-2542.
(25) Silaghi, M.-C.; Chizallet, C.; Raybaud, P., Challenges on Molecular Aspects of Dealumination and Desilication of Zeolites, *Microporous Mesoporous Mater.* **2014**, *191*, 82-96.
(26) Pagis, C.; Morgado Prates, A. R.; Farrusseng, D.; Bats, N.; Tuel, A., Hollow Zeolite Structures: An Overview of Synthesis Methods, *Chem. Mater.* **2016**, *28*, 5205-5223.
(27) Corma, A.; Fornes, V.; Pergher, S. B.; Maesen, T. L. M.; Buglass, J. G., Delaminated Zeolite Precursors as Selective Acidic Catalysts, *Nature* **1998**, *396*, 353.
(28) Choi, M.; Na, K.; Kim, J.; Sakamoto, Y.; Terasaki, O.; Ryoo, R., Stable Single-Unit-Cell Nanosheets of Zeolite MFI as Active and Long-Lived Catalysts, *Nature* **2009**, *461*, 246-249.
(29) Roth, W. J.; Nachtigall, P.; Morris, R. E.; Čejka, J., Two-Dimensional Zeolites: Current Status and Perspectives, *Chem. Rev.* **2014**, *114*, 4807-4837.
(30) Argauer, R. J.; Landolt, G. R.; Mobil Oil Corporation: US 3702886, 1972.
(31) Pelrine, B. P.; Mobil Oil Corporation: US 4100262, 1978.
(32) Rollman, L. D.; Valyocsik, E. W.; Corporation, M. O., Ed. EP 0021674, 1980.
(33) Kokotailo, G. T.; Lawton, S. L.; Olson, D. H.; Meier, W. M., Structure of Synthetic Zeolite ZSM-5, *Nature* **1978**, *272*, 437.
(34) Flanigen, E. M.; Bennett, J. M.; Grose, R. W.; Cohen, J. P.; Patton, R. L.; Kirchner, R. M.; Smith, J. V., Silicalite, a New Hydrophobic Crystalline Silica Molecular Sieve, *Nature* **1978**, *271*, 512-516.
(35) Cundy, C. S.; Cox, P. A., The Hydrothermal Synthesis of Zeolites: History and Development from the Earliest Days to the Present Time, *Chem. Rev.* **2003**, *103*, 663-702.
(36) Pereira, M. M.; Gomes, E. S.; Silva, A. V.; Pinar, A. B.; Willinger, M.-G.; Shanmugam, S.; Chizallet, C.; Laugel, G.; Losch, P.; Louis, B., Biomass-Mediated ZSM-5 Zeolite Synthesis: When Self-Assembly Allows to Cross the Si/Al Lower Limit, *Chem. Sci.* **2018**, *9*, 6532-6539.
(37) Lermer, H.; Draeger, M.; Steffen, J.; Unger, K. K., Synthesis and Structure Refinement of ZSM-5 Single Crystals, *Zeolites* **1985**, *5*, 131-134.
(38) Fyfe, C. A.; Kennedy, G. J.; De Schutter, C. T.; Kokotailo, G. T., Sorbate-Induced Structural Changes in ZSM-5 (Silicalite), *J. Chem. Soc., Chem. Commun.* **1984**, 541-542.
(39) Hay, D. G.; Jaeger, H., Orthorhombic-Monoclinic Phase Changes in ZSM-5 Zeolite/Silicalite, *J. Chem. Soc., Chem. Commun.* **1984**, 1433-1433.

(40) Kirschhock, C. E. A.; Buschmann, V.; Kremer, S.; Ravishankar, R.; Houssin, C. J. Y.; Mojet, B. L.; van Santen, R. A.; Grobet, P. J.; Jacobs, P. A.; Martens, J. A., Zeosil Nanoslabs: Building Blocks in nPr_4N^+-Mediated Synthesis of MFI Zeolite, *Angew. Chem. Int. Ed.* **2001**, *40*, 2637-2640.
(41) Kirschhock, C. E. A.; Ravishankar, R.; Looveren, L. V.; Jacobs, P. A.; Martens, J. A., Mechanism of Transformation of Precursors into Nanoslabs in the Early Stages of MFI and MEL Zeolite Formation from TPAOH−TEOS−H_2O and TBAOH−TEOS−H_2O Mixtures, *J. Phys. Chem. B* **1999**, *103*, 4972-4978.
(42) Knight, C. T. G.; Kinrade, S. D., Comment on "Identification of Precursor Species in the Formation of MFI Zeolite in the TPAOH−TEOS−H_2O System", *J. Phys. Chem. B* **2002**, *106*, 3329-3332.
(43) Kirschhock, C. E. A.; Ravishankar, R.; Verspeurt, F.; Grobet, P. J.; Jacobs, P. A.; Martens, J. A., Reply to the Comment on "Identification of Precursor Species in the Formation of MFI Zeolite in the TPAOH−TEOS−H_2O System", *J. Phys. Chem. B* **2002**, *106*, 3333-3334.
(44) Davis, T. M.; Drews, T. O.; Ramanan, H.; He, C.; Dong, J.; Schnablegger, H.; Katsoulakis, M. A.; Kokkoli, E.; McCormick, A. V.; Penn, R. L.; Tsapatsis, M., Mechanistic Principles of Nanoparticle Evolution to Zeolite Crystals, *Nat. Mater.* **2006**, *5*, 400.
(45) Cundy, C. S.; Cox, P. A., The Hydrothermal Synthesis of Zeolites: Precursors, Intermediates and Reaction Mechanism, *Microporous Mesoporous Mater.* **2005**, *82*, 1-78.
(46) Lupulescu, A. I.; Rimer, J. D., In Situ Imaging of Silicalite-1 Surface Growth Reveals the Mechanism of Crystallization, *Science* **2014**, *344*, 729.
(47) Kumar, S.; Wang, Z.; Penn, R. L.; Tsapatsis, M., A Structural Resolution Cryo-TEM Study of the Early Stages of MFI Growth, *J. Am. Chem. Soc.* **2008**, *130*, 17284-17286.
(48) Burel, L.; Tuel, A., Nanozeolites: New Strategies for Designing Ultra Small Silicalite Crystals with Very Few Framework Defects, *Microporous Mesoporous Mater.* **2013**, *174*, 90-99.
(49) Gruene, T.; Li, T.; van Genderen, E.; Pinar, A. B.; van Bokhoven, J. A., Characterization at the Level of Individual Crystals: Single-Crystal MFI Type Zeolite Grains, *Chem. Eur. J.* **2018**, *24*, 2384-2388.
(50) Koegler, J. H.; van Bekkum, H.; Jansen, J. C., Growth Model of Oriented Crystals of Zeolite Si-ZSM-5, *Zeolites* **1997**, *19*, 262-269.
(51) Roeffaers, M. B. J.; Ameloot, R.; Baruah, M.; Uji-i, H.; Bulut, M.; De Cremer, G.; Müller, U.; Jacobs, P. A.; Hofkens, J.; Sels, B. F.; De Vos, D. E., Morphology of Large ZSM-5 Crystals Unraveled by Fluorescence Microscopy, *J. Am. Chem. Soc.* **2008**, *130*, 5763–5772.
(52) Price, G. D.; Pluth, J. J.; Smith, J. V.; Bennett, J. M.; Patton, R. L., Crystal Structure of Tetrapropylammonium Fluoride-Containing Precursor to Fluoride Silicalite, *J. Am. Chem. Soc.* **1982**, *104*, 5971-5977.
(53) Millward, G. R.; Ramdas, S.; Thomas, J. M.; Barlow, M. T., Evidence for Semi-Regularly Ordered Sequences of Mirror and Inversion Symmetry Planes in ZSM-5/ZSM-11 Shape-Selective Zeolitic Catalysts, *J. Chem. Soc., Faraday Trans. 2* **1983**, *79*, 1075-1082.
(54) Hay, D. G.; Jaeger, H.; Wilshier, K. G., Systematic Intergrowth in Crystals of ZSM-5 Zeolite, *Zeolites* **1990**, *10*, 571-576.
(55) Weidenthaler, C.; Fischer, R. X.; Shannon, R. D.; Medenbach, O., Optical Investigations of Intergrowth Effects in the Zeolite Catalysts ZSM-5 and ZSM-8, *J. Phys. Chem.* **1994**, *98*, 12687-12694.
(56) Agger, J. R.; Hanif, N.; Cundy, C. S.; Wade, A. P.; Dennison, S.; Rawlinson, P. A.; Anderson, M. W., Silicalite Crystal Growth Investigated by Atomic Force Microscopy, *J. Am. Chem. Soc.* **2003**, *125*, 830-839.
(57) Karwacki, L.; Kox, M. H. F.; Matthijs de Winter, D. A.; Drury, M. R.; Meeldijk, J. D.; Stavitski, E.; Schmidt, W.; Mertens, M.; Cubillas, P.; John, N.; Chan, A.; Kahn, N.; Bare, S. R.; Anderson, M.; Kornatowski, J.; Weckhuysen, B. M., Morphology-Dependent Zeolite Intergrowth Structures Leading to Distinct Internal and Outer-Surface Molecular Diffusion Barriers, *Nat. Mater.* **2009**, *8*, 959.
(58) Stavitski, E.; Drury, M. R.; de Winter, D. A. M.; Kox, M. H. F.; Weckhuysen, B. M., Intergrowth Structure of Zeolite Crystals and Pore Orientation of Individual Subunits Revealed by Electron Backscatter Diffraction/Focused Ion Beam Experiments, *Angew. Chem. Int. Ed.* **2008**, *47*, 5637-5640.
(59) Roeffaers, M. B. J.; Ameloot, R.; Bons, A.-J.; Mortier, W.; De Cremer, G.; de Kloe, R.; Hofkens, J.; De Vos, D. E.; Sels, B. F., Relating Pore Structure to Activity at the Subcrystal Level for ZSM-5: An Electron Backscattering Diffraction and Fluorescence Microscopy Study, *J. Am. Chem. Soc.* **2008**, *130*, 13516-13517.
(60) Zeng, G.; Chen, C.; Li, D.; Hou, B.; Sun, Y., Exposure of (001) Planes and (011) Planes in MFI Zeolite, *CrystEngComm* **2013**, *15*, 3521-3524.
(61) Díaz, I.; Kokkoli, E.; Terasaki, O.; Tsapatsis, M., Surface Structure of Zeolite (MFI) Crystals, *Chem. Mater.* **2004**, *16*, 5226-5232.
(62) Varoon, K.; Zhang, X.; Elyassi, B.; Brewer, D. D.; Gettel, M.; Kumar, S.; Lee, J. A.; Maheshwari, S.; Mittal, A.; Sung, C.-Y.; Cococcioni, M.; Francis, L. F.; McCormick, A. V.; Mkhoyan, K. A.; Tsapatsis, M., Dispersible Exfoliated Zeolite Nanosheets and Their Application as a Selective Membrane, *Science* **2011**, *334*, 72.
(63) Zhang, X.; Liu, D.; Xu, D.; Asahina, S.; Cychosz, K. A.; Agrawal, K. V.; Al Wahedi, Y.; Bhan, A.; Al Hashimi, S.; Terasaki, O.; Thommes, M.; Tsapatsis, M., Synthesis of Self-Pillared Zeolite Nanosheets by Repetitive Branching, *Science* **2012**, *336*, 1684.
(64) Shete, M.; Kumar, M.; Kim, D.; Rangnekar, N.; Xu, D.; Topuz, B.; Agrawal, K. V.; Karapetrova, E.; Stottrup, B.; Al-Thabaiti, S.; Basahel, S.; Narasimharao, K.; Rimer, J. D.; Tsapatsis, M., Nanoscale Control of Homoepitaxial Growth on a Two-Dimensional Zeolite, *Angew. Chem. Int. Ed.* **2017**, *56*, 535-539.
(65) Jeon, M. Y.; Kim, D.; Kumar, P.; Lee, P. S.; Rangnekar, N.; Bai, P.; Shete, M.; Elyassi, B.; Lee, H. S.; Narasimharao, K.; Basahel, S. N.; Al-Thabaiti, S.; Xu, W.; Cho, H. J.; Fetisov, E. O.; Thyagarajan, R.; DeJaco, R. F.; Fan, W.; Mkhoyan, K. A.; Siepmann, J. I.; Tsapatsis, M., Ultra-Selective High-Flux Membranes from Directly Synthesized Zeolite Nanosheets, *Nature* **2017**, *543*, 690-694.
(66) Hernandez-Tamargo, C. E.; Roldan, A.; de Leeuw, N. H., A Density Functional Theory Study of the Structure of Pure-Silica and Aluminium-Substituted MFI Nanosheets, *J. Solid State Chem.* **2016**, *237*, 192-203.
(67) Zhai, D.; Liu, Y.; Zheng, H.; Zhao, L.; Gao, J.; Xu, C.; Shen, B., A First-Principles Evaluation of the Stability, Accessibility, and Strength of Brønsted Acid Sites in Zeolites, *J. Catal.* **2017**, *352*, 627-637.

(68) Rybicki, M.; Sauer, J., Acid Strength of Zeolitic Brønsted Sites—Dependence on Dielectric Properties, *Catal. Today* **2019**, *323*, 86-93.
(69) Ho, T. V.; Nachtigall, P.; Grajciar, L., The Lewis Acidity of Three- and Two-Dimensional Zeolites: The Effect of Framework Topology, *Catal. Today* **2018**, *304*, 12-21.
(70) Thang, H. V.; Vaculík, J.; Přech, J.; Kubů, M.; Čejka, J.; Nachtigall, P.; Bulánek, R.; Grajciar, L., The Brønsted acidity of three- and two-dimensional zeolites, *Microporous Mesoporous Mater.* **2019**, *282*, 121-132.
(71) Prestianni, A.; Cortese, R.; Duca, D., Propan-2-ol Dehydration on H-ZSM-5 and H-Y zeolite: a DFT Study, *React. Kinet. Catal.* **2013**, *108*, 565-582.
(72) Ferrante, F.; Rubino, T.; Duca, D., Butene Isomerization and Double-Bond Migration on the H-ZSM-5 Outer Surface: A Density Functional Theory Study, *J. Phys. Chem. C* **2011**, *115*, 14862-14868.
(73) van Bokhoven, J. A.; van der Eerden, A. M. J.; Koningsberger, D. C., Three-Coordinate Aluminum in Zeolites Observed with In situ X-ray Absorption Near-Edge Spectroscopy at the Al K-Edge: Flexibility of Aluminum Coordinations in Zeolites, *J. Am. Chem. Soc.* **2003**, *125*, 7435-7442.
(74) Brus, J.; Kobera, L.; Schoefberger, W.; Urbanova, M.; Klein, P.; Sazama, P.; Tabor, E.; Sklenak, S.; Fishchuk, A. V.; Dedecek, J., Structure of Framework Aluminum Lewis sites and Perturbed Aluminum atoms in Zeolites as Determined by ^{27}Al{^{1}H} REDOR (3Q) MAS NMR Spectroscopy and DFT/Molecular Mechanics, *Angew. Chem. Int. Ed.* **2015**, *54*, 541-545.
(75) Ravi, M.; Sushkevich, V. L.; van Bokhoven, J. A., Lewis Acidity Inherent to the Framework of Zeolite Mordenite, *J. Phys. Chem. C* **2019**, *123*, 15139-15144.
(76) Phung, T. K.; Busca, G., On the Lewis Acidity of Protonic Zeolites, *Appl. Catal. A* **2015**, *504*, 151-157.
(77) Derouane, E. G.; Védrine, J. C.; Pinto, R. R.; Borges, P. M.; Costa, L.; Lemos, M. A. N. D. A.; Lemos, F.; Ribeiro, F. R., The Acidity of Zeolites: Concepts, Measurements and Relation to Catalysis: A Review on Experimental and Theoretical Methods for the Study of Zeolite Acidity, *Catal. Rev.* **2013**, *55*, 454-515.
(78) Perdew, J.; Burke, K.; Ernzerhof, M., Generalized Gradient Approximation Made Simple, *Phys. Rev. Lett.* **1996**, *77*, 3865-3868.
(79) Kresse, G.; Hafner, J., Ab Initio Molecular-Dynamics Simulation of the Liquid-Metal-Amorphous-Semiconductor Transition in Germanium, *Phys. Rev. B* **1994**, *49*, 14251-14269.
(80) Kresse, G.; Furthmüller, J., Efficiency of Ab-Initio Total Energy Calculations for Metals and Semiconductors using a Plane-Wave Basis Set, *Comput. Mat. Sci.* **1996**, *6*, 15-50.
(81) Kresse, G.; Joubert, D., From Ultrasoft Pseudopotentials to the Projector Augmented-Wave Method, *Phys. Rev. B* **1999**, *59*, 1758-1775.
(82) Steinmann, S. N.; Corminboeuf, C., Comprehensive Benchmarking of a Density-Dependent Dispersion Correction, *J Chem Theory Comput* **2011**, *7*, 3567-3577.
(83) Wu, E. L.; Lawton, S. L.; Olson, D. H.; Rohrman, A. C.; Kokotailo, G. T., ZSM-5-Type Materials. Factors Affecting Crystal Symmetry, *J. Phys. Chem.* **1979**, *83*, 2777-2781.
(84) Olson, D. H.; Kokotailo, G. T.; Lawton, S. L.; Meier, W. M., Crystal Structure and Structure-Related Properties of ZSM-5, *J. Phys. Chem.* **1981**, *85*, 2238-2243.
(85) Reuter, K.; Scheffler, M., Composition, Structure, and Stability of RuO_2(110) as a Function of Oxygen Pressure, *Phys. Rev. B* **2001**, *65*, 035406.
(86) Larmier, K.; Chizallet, C.; Cadran, N.; Maury, S.; Abboud, J.; Lamic-Humblot, A.-F.; Marceau, E.; Lauron-Pernot, H., Mechanistic Investigation of Isopropanol Conversion on Alumina Catalysts: Location of Active Sites for Alkene/Ether Production, *ACS Catal.* **2015**, *5*, 4423-4437.
(87) Rey, J.; Raybaud, P.; Chizallet, C., Ab Initio Simulation of the Acid Sites at the External Surface of Zeolite Beta, *ChemCatChem* **2017**, *9*, 2176-2185.
(88) Musso, F.; Sodupe, M.; Corno, M.; Ugliengo, P., H-Bond Features of Fully Hydroxylated Surfaces of Crystalline Silica Polymorphs: A Periodic B3LYP Study, *J. Phys. Chem. C* **2009**, *113*, 17876-17884.
(89) Witman, M.; Ling, S.; Boyd, P.; Barthel, S.; Haranczyk, M.; Slater, B.; Smit, B., Cutting Materials in Half: A Graph Theory Approach for Generating Crystal Surfaces and Its Prediction of 2D Zeolites, *ACS central science* **2018**, *4*, 235-245.
(90) Seo, Y.; Cho, K.; Jung, Y.; Ryoo, R., Characterization of the Surface Acidity of MFI Zeolite Nanosheets by ^{31}P NMR of Adsorbed Phosphine Oxides and Catalytic Cracking of Decalin, *ACS Catal.* **2013**, *3*, 713-720.
(91) Curie, P., Sur la Formation des Cristaux et sur les Constantes Capillaires de leurs Différentes Faces, *Bulletin de Minéralogie* **1885**, 145-150.
(92) Wulff, G., Zur Frage der Geschwindigkeit des Wachsthums und der Auflösung der Krystallflächen, *Zeitschrift f. Krystallogr.* **1901**, *34*, 449-530.
(93) Baumgärtl, M.; Jentys, A.; Lercher, J. A., Understanding Elementary Steps of Transport of Xylene Mixtures in ZSM-5 Zeolites, *J. Phys. Chem. C* **2018**, *123*, 8092-8100.
(94) Liang, D.; Follens, L. R. A.; Aerts, A.; Martens, J. A.; Van Tendeloo, G.; Kirschhock, C. E. A., TEM Observation of Aggregation Steps in Room-Temperature Silicalite-1 Zeolite Formation, *J. Phys. Chem. C* **2007**, *111*, 14283-14285.
(95) Rohling, R. Y.; Szyja, B. M.; Hensen, E. J. M., Insight into the Formation of Nanostructured MFI Sheets and MEL Needles Driven by Molecular Recognition, *The journal of physical chemistry. C, Nanomaterials and interfaces* **2019**, *123*, 5326-5335.
(96) Piccione, P. M.; Yang, S.; Navrotsky, A.; Davis, M. E., Thermodynamics of Pure-Silica Molecular Sieve Synthesis, *J. Phys. Chem. B* **2002**, *106*, 3629-3638.
(97) Corma, A.; Davis, M. E., Issues in the Synthesis of Crystalline Molecular Sieves: Towards the Crystallization of Low Framework-Density Structures, *ChemPhysChem* **2004**, *5*, 304-313.

(98) Wang, S.; He, Y.; Jiao, W.; Wang, J.; Fan, W., Recent Experimental and Theoretical Studies on Al Siting/Acid Site Distribution in Zeolite Framework, *Curr. Opin. Chem. Eng.* **2019**, *23*, 146-154.
(99) Muraoka, K.; Chaikittisilp, W.; Okubo, T., Energy Analysis of Aluminosilicate Zeolites with Comprehensive Ranges of Framework Topologies, Chemical Compositions, and Aluminum Distributions, *J. Am. Chem. Soc.* **2016**, *138*, 6184-6193.
(100) Schröder, K.-P.; Sauer, J.; Leslie, M.; A.Catlow, C. R., Siting of AI and Bridging Hydroxyl Groups in ZSM-5: A Computer Simulation Study, *Zeolites* **1992**, *12*, 20-23.
(101) Li, C.; Vidal-Moya, A.; Miguel, P. J.; Dedecek, J.; Boronat, M.; Corma, A., Selective Introduction of Acid Sites in Different Confined Positions in ZSM-5 and Its Catalytic Implications, *ACS Catal.* **2018**, *8*, 7688-7697.
(102) Dib, E.; Mineva, T.; Gaveau, P.; Véron, E.; Sarou-Kanian, V.; Fayon, F.; Alonso, B., Probing Disorder in Al-ZSM-5 Zeolites by 14N NMR Spectroscopy, *J. Phys. Chem. C* **2017**, *121*, 15831-15841.
(103) Knott, B. C.; Nimlos, C. T.; Robichaud, D. J.; Nimlos, M. R.; Kim, S.; Gounder, R., Consideration of the Aluminum Distribution in Zeolites in Theoretical and Experimental Catalysis Research, *ACS Catal.* **2017**, *8*, 770-784.
(104) Bucko, T.; Benco, L.; Demuth, T.; Hafner, J., Ab Initio Density Functional Investigation of the (001) Surface of Mordenite, *J. Chem. Phys.* **2002**, *117*, 7295-7305.
(105) Demuth, T.; Hafner, J.; Benco, L.; Toulhoat, H., Structural and Acidic Properties of Mordenite. An ab Initio Density-Functional Study, *J. Phys. Chem. B* **2000**, *104*, 4593-4607.
(106) Gutierrez-Acebo, E.; Rey, J.; Bouchy, C.; Schuurman, Y.; Chizallet, C., Location of the Active Sites for Ethylcyclohexane Hydroisomerization by Ring Contraction and Expansion in the EUO Zeolitic Framework, *ACS Catal.* **2019**, *9*, 1692-1704.
(107) Ghorbanpour, A.; Rimer, J. D.; Grabow, L. C., Periodic, vdW-Corrected Density Functional Theory Investigation of the Effect of Al Siting in H-ZSM-5 on Chemisorption Properties and Site-Specific Acidity, *Catal. Comm.* **2014**, *52*, 98-102.
(108) Dib, E.; Mineva, T.; Veron, E.; Sarou-Kanian, V.; Fayon, F.; Alonso, B., ZSM-5 Zeolite: Complete Al Bond Connectivity and Implications on Structure Formation from Solid-State NMR and Quantum Chemistry Calculations, *J Phys Chem Lett* **2018**, *9*, 19-24.
(109) Silaghi, M.-C.; Chizallet, C.; Petracovschi, E.; Kerber, T.; Sauer, J.; Raybaud, P., Regioselectivity of Al-O Bond Hydrolysis During Zeolites Dealumination Unified by Brønsted-Evans-Polanyi Relationship, *ACS Catal.* **2015**, *5*, 11-15.
(110) Silaghi, M.-C.; Chizallet, C.; Sauer, J.; Raybaud, P., Dealumination Mechanisms of Zeolites and Extra-Framework Aluminum Confinement, *J. Catal.* **2016**, *339*, 242-255.
(111) Holzinger, J.; Beato, P.; Lundegaard, L. F.; Skibsted, J., Distribution of Aluminum over the Tetrahedral Sites in ZSM-5 Zeolites and Their Evolution after Steam Treatment, *J. Phys. Chem. C* **2018**, *122*, 15595-15613.
(112) Han, O. H.; Kim, C. S.; Hong, S. B., Direct Evidence for the Nonrandom Nature of Al Substitution in Zeolite ZSM-5: An Investigation by ^{27}Al MAS and MQ MAS NMR, *Angew. Chem. Int. Ed.* **2002**, *41*, 469-472.
(113) Sklenak, S.; Dedecek, J.; Li, C.; Wichterlova, B.; Gabova, V.; Sierka, M.; Sauer, J., Aluminum Siting in Silicon-Rich Zeolite Frameworks: A Combined High-Resolution ^{27}Al NMR Spectroscopy and Quantum Mechanics/Molecular Mechanics Study of ZSM-5, *Angew. Chem., Int. Ed* **2007**, *46*, 7286-7289.
(114) Dědeček, J.; Sobalík, Z.; Wichterlová, B., Siting and Distribution of Framework Aluminium Atoms in Silicon-Rich Zeolites and Impact on Catalysis, *Catal. Rev.* **2012**, *54*, 135-223.
(115) Bucko, T.; Benco, L.; Hafner, J., Defect Sites at the .001. Surface of Mordenite: An Ab Initio Study, *J. Chem. Phys.* **2003**, *118*, 8437-8445.
(116) Busca, G., Catalytic Materials Based on Silica and Alumina: Structural Features and Generation of Surface Acidity, *Prog. Mater. Sci.* **2019**, *104*, 215-249.
(117) Bevilacqua, M.; Montanari, T.; Finocchio, E.; Busca, G., Are the Active Sites of Protonic Zeolites Generated by the Cavities?, *Catal. Today* **2006**, *116*, 132-142.
(118) von Ballmoos, R.; Meier, W. M., Zoned Aluminium Distribution in Synthetic Zeolite ZSM-5, *Nature* **1981**, *289*, 782-783.
(119) Maciel, G. E.; Sindorf, D. W., Silicon-29 NMR Study of the Surface of Silica Gel by Cross Polarization and Magic-Angle Spinning, *J. Am. Chem. Soc.* **1980**, *102*, 7606-7607.
(120) Drake, I. J.; Zhang, Y.; Gilles, M. K.; Teris Liu, C. N.; Nachimuthu, P.; Perera, R. C. C.; Wakita, H.; Bell, A. T., An In Situ Al K-Edge XAS Investigation of the Local Environment of H^+- and Cu^+-Exchanged USY and ZSM-5 Zeolites, *J. Phys. Chem. B* **2006**, *110*, 11665-11676.
(121) Lonstad Bleken, B.-T.; Mino, L.; Giordanino, F.; Beato, P.; Svelle, S.; Lillerud, K. P.; Bordiga, S., Probing the Surface of Nanosheet H-ZSM-5 with FTIR Spectroscopy, *Phys. Chem. Chem. Phys.* **2013**, *15*, 13363-13370.
(122) Knözinger, H.,Infrared Spectroscopy for the Characterization of Surface Acidity and Basicity, In *Handbook of Heterogeneous Catalysis*; Ertl, G., Knözinger, H., Weitkamp, J., Eds.; Wiley: Weinheim, 1997; Vol. 2, p 707-732.
(123) Bordiga, S.; Lamberti, C.; Bonino, F.; Travert, A.; Thibault-Starzyk, F., Probing Zeolites by Vibrational Spectroscopies, *Chem. Soc. Rev.* **2015**, *44*, 7262-7341.
(124) Zhang, N.; Liu, C.; Ma, J.; Li, R.; Jiao, H., Determining the Structures, Acidity and Adsorption Properties of Al Substituted HZSM-5, *Phys. Chem. Chem. Phys.* **2019**, *21*, 18758-18768.
(125) Lee, C.; Parrillo, D. J.; Gorte, R. J.; Farneth, W. E., Relationship between Differential Heats of Adsorption and Brønsted Acid Strengths of Acidic Zeolites: H-ZSM-5 and H-Mordenite, *J. Am. Chem. Soc.* **1996**, *118*, 3262-3268.
(126) Jin, F.; Li, Y., A FTIR and TPD Examination of the Distributive Properties of Acid Sites on ZSM-5 Zeolite with Pyridine as a Probe Molecule, *Catal. Today* **2009**, *145*, 101-107.
(127) Leydier, F.; Chizallet, C.; Chaumonnot, A.; Digne, M.; Soyer, E.; Quoineaud, A. A.; Costa, D.; Raybaud, P., Brønsted Acidity of Amorphous Silica–Alumina: The Molecular Rules of Proton Transfer, *J. Catal.* **2011**, *284*, 215-229.

(128) Chizallet, C.; Raybaud, P., Pseudo-Bridging Silanols as Versatile Brønsted Acid Sites of Amorphous Aluminosilicates Surfaces, *Angew. Chem. Int. Ed.* **2009**, *48*, 2891-2893.
(129) Trombetta, M.; Armaroli, T.; Gutièrrez Alejandre, A. d.; Ramirez Solis, J.; Busca, G., An FT-IR study of the Internal and External Surfaces of HZSM5 Zeolite, *Appl. Catal. A* **2000**, *192*, 125-136.
(130) Opanasenko, M. V.; Shamzhy, M. V.; Jo, C.; Ryoo, R.; Čejka, J., Annulation of Phenols: Catalytic Behavior of Conventional and 2 D Zeolites, *ChemCatChem* **2014**, *6*, 1919-1927.
(131) Bolton, A. P.; Lanewala, M. A., Thermochemical Reactions of Ammonium-Exchanged Y Zeolite and its Derivatives, *J. Catal.* **1970**, *18*, 154-163.
(132) Louis, B.; Vicente, A. l.; Fernandez, C.; Valtchev, V., Crystal Size–Acid Sites Relationship Study of Nano- and Micrometer-Sized Zeolite Crystals, *J. Phys. Chem. C* **2011**, *115*, 18603-18610.
(133) Thibault-Starzyk, F.; Stan, I.; Abello, S.; Bonilla, A.; Thomas, K.; Fernadez, C.; Gilson, J. P.; Perez-Ramirez, J., Quantification of Enhanced Acid Site Accessibility in Hierarchical Zeolites – The Accessibility Index, *J. Catal.* **2009**, *264*, 11-14.
(134) Leydier, F.; Chizallet, C.; Costa, D.; Raybaud, P., Revisiting Carbenium Chemistry on Amorphous Silica-Alumina: Unraveling their Milder Acidity as Compared to Zeolites, *J. Catal.* **2015**, *325*, 35-47.
(135) Valla, M.; Rossini, A. J.; Caillot, M.; Chizallet, C.; Raybaud, P.; Digne, M.; Chaumonnot, A.; Lesage, A.; Emsley, L.; van Bokhoven, J. A.; Coperet, C., Atomic Description of the Interface between Silica and Alumina in Aluminosilicates through Dynamic Nuclear Polarization Surface-Enhanced NMR Spectroscopy and First-Principles Calculations, *J. Am. Chem. Soc.* **2015**, *137*, 10710-10719.
(136) Larmier, K.; Chizallet, C.; Maury, S.; Cadran, N.; Abboud, J.; Lamic-Humblot, A. F.; Marceau, E.; Lauron-Pernot, H., Isopropanol Dehydration on Amorphous Silica-Alumina: Synergy of Bronsted and Lewis Acidities at Pseudo-Bridging Silanols, *Angew. Chem. Int. Ed.* **2017**, *56*, 230-234.